Tracking Calcium Dynamics and Immune Surveillance at the Choroid Plexus Blood-Cerebrospinal Fluid Interface

Frederick B Shipley, Neil Dani, Huixin Xu, Christopher Deister, Jin Cui, Joshua P Head, Cameron Sadegh, Ryann M Fame, Morgan L Shannon, Vanessa I Flores, et al.

Tracking calcium dynamics and immune surveillance at the choroid plexus blood-cerebrospinal fluid interface

Frederick B. Shipley,[1,2,*] Neil Dani,[1,*] Huixin Xu,[1] Christopher Deister,[3] Jin Cui,[1] Joshua P. Head,[1] Cameron Sadegh,[1,4] Ryann M. Fame,[1] Morgan L. Shannon,[1] Vanessa I. Flores,[5] Thomas Kishkovich,[3] Emily Jang,[3] Eric M. Klein,[3] Glenn J. Goldey,[5] Kangmin He,[6,9] Yong Zhang,[7] Michael J. Holtzman,[7] Tomas Kirchhausen,[6] Claire Wyart,[8] Christopher I. Moore,[3] Mark L. Andermann,[2,5,#] Maria K. Lehtinen[1,2,#]

[1]Department of Pathology, Boston Children's Hospital, Boston, MA 02115, USA
[2]Graduate Program in Biophysics, Harvard University, Cambridge, MA 02138, USA
[3]Carney Institute for Brain Science, Brown University, Providence, RI 02912, USA
[4]Department of Neurosurgery, Massachusetts General Hospital, Harvard Medical School, Boston, MA 02114, USA
[5]Division of Endocrinology, Diabetes, and Metabolism, Department of Medicine, Beth Israel Deaconess Medical Center, Boston, MA 02115, USA
[6]Department of Cell Biology and Department of Pediatrics, Harvard Medical School, Program in Cellular and Molecular Medicine, Boston Children's Hospital, Boston, MA 02115, USA
[7]Pulmonary and Critical Care Medicine, Department of Medicine, Washington University, St. Louis, MO 63110, USA
[8]Institut du Cerveau et de la Moelle épinière (ICM), Sorbonne Université, Inserm U1127, CNRS UMR 7225, Paris 75013, France
[9]Present Address: National Laboratory of Biomacromolecules, Institute of Biophysics, Chinese Academy of Sciences, Beijing 100101, China
* These authors contributed equally
# Co-senior authors
Lead contact: maria.lehtinen@childrens.harvard.edu
Corresponding authors: manderma@bidmc.harvard.edu; maria.lehtinen@childrens.harvard.edu

SUMMARY

The choroid plexus (ChP) epithelium is a source of secreted signaling factors in cerebrospinal fluid (CSF) and a key barrier between blood and brain. Here, we develop imaging tools to interrogate these functions in adult lateral ventricle ChP in wholemount explants and in awake mice. By imaging epithelial cells in intact ChP explants, we observed calcium activity and secretory events that increased in frequency following delivery of serotonergic agonists. Using chronic two-photon imaging in awake mice, we observed spontaneous subcellular calcium events as well as strong agonist-evoked calcium activation and cytoplasmic secretion into CSF. Three-dimensional imaging of motility and mobility of multiple types of ChP immune cells at baseline and following immune challenge or focal injury revealed a range of surveillance and defensive behaviors. Together, these tools should help illuminate the diverse functions of this understudied body-brain interface.

KEYWORDS

Choroid plexus, cerebrospinal fluid, two-photon imaging, calcium activity, serotonin, secretion, epithelial cells, immune cells

INTRODUCTION

The choroid plexus (ChP) is a distinct, vital organ that extends into each ventricle in the brain. It is composed predominantly of epithelial cells that envelop a network of stromal cell types including immune, mesenchymal, and vascular cells (Dani et al., 2019). The epithelial cells provide a source of cerebrospinal fluid (CSF) (Damkier et al., 2013) and associated growth-promoting factors for neural stem cells (Lehtinen et al., 2011; Fame and Lehtinen, 2020; Silva-Vargas et al., 2016). They also form a blood-CSF barrier that gates passage of nutrients, toxins, and immune cells from body to brain (Ghersi-Egea et al., 2018; Reboldi et al., 2009; Schwartz and Baruch, 2014; Shechter et al., 2013), and may regulate CSF composition via clearance of toxins and waste (Crossgrove et al., 2005). Thus, the sensing, secretory, and transcytotic functions of the ChP suggest diverse roles in regulating brain function. These roles may be disrupted in neurologic conditions ranging from hydrocephalus (Karimy et al., 2017) to Alzheimer's disease (Balusu et al., 2016a; Marques et al., 2013). Further, the ChP is an attractive target for enhancing drug delivery to the brain (Gonzalez et al., 2011; Haddad et al., 2013; Hudry and Vandenberghe, 2019).

Despite the importance of the ChP-CSF system, little is known about the behavior of mammalian ChP cell types *in vivo*. *In vitro* approaches exist for culturing ChP cell lines (Zheng and Zhao, 2002), dissociated ChP cells (Zheng et al., 1998), ChP epithelial cell sheets in transwell models (Strazielle and Ghersi-Egea, 1999), and ChP organoids (Pellegrini et al., 2020; Watanabe et al., 2012). Isolated ChP explants have also been used for analyzing secretion into conditioned medium (Gudeman et al., 1987, 1989; Lun et al., 2015a; Silva-Vargas et al., 2016), or for fixation and immunostaining (Dani et al., 2019; Lun et al., 2015a). Anatomical studies using light and electron microscopy (EM) have provided clues as to the cellular architecture of

the ChP (e.g. Netsky and Shuangshoti, 1975). However, a major obstacle to progress in understanding the roles of ChP cells has been the lack of available tools for stable visualization and manipulation of specific ChP cell types in intact tissue *in vitro* and *in vivo* in a fluid environment deep within the brain.

Here, we adapted a suite of modern neuroscience tools to target the lateral ventricle ChP, providing optical access to this unexplored tissue in mice. We developed methods for volumetric two-photon imaging and non-rigid alignment of the ChP in acute explant preparations, as well as in awake mice across hours, days, and weeks. Dynamic cellular functions of other epithelia (e.g. in retina, lung, and salivary gland) are typically associated with changes in intracellular calcium (Ambudkar, 2016; Balaji et al., 2017; Concepcion and Feske, 2017; Narciso et al., 2017; Samanta and Parekh, 2016). For example, calcium signaling in salivary gland is important for on-demand secretion (Ambudkar, 2018, 2016). We found that ChP epithelial cells exhibited spontaneous subcellular calcium activity *in vitro* and *in vivo.* Serotonergic agonists evoked distributed increases in calcium activity, as well as secretory events measured using a sensor of exocytosis. We then visualized the motility and mobility of ChP immune cells in relation to ChP vasculature in awake mice at baseline and in response to peripheral immune stimulation and to laser-induced, focal ChP injury. Together, these methods provide a novel imaging platform for a wide range of studies imaging multiple genetically accessible ChP cell types in intact tissue at unprecedented spatial and temporal resolution.

RESULTS

Imaging ChP explants

We first optimized adult lateral ventricle (LV) ChP explant preparations (Dani et al., 2019; Lun et al., 2015a) to enable histological analyses (**Figures 1A-1D**) and stable live-cell imaging (**Figures 1E, 1F, and S1A**). Epithelial cells constitute the majority of adult ChP cells (Dani et al., 2019). In addition, the ChP contains immune cells (labeled by *Cx3cr1*$^{+/GFP}$ (Jung et al., 2000)) consisting mostly of monocytes/macrophages but also including a smaller number of mast cells and dendritic cells (Dani et al., 2019; Van Hove et al., 2019). These immune cells evenly tiled the entire tissue under baseline conditions (**Figures 1A-1C**). The ChP could be divided into stereotyped zones defined by arterial and venous landmarks (**Figures 1D, S1B, and S1C**) (Dani et al., 2019). This vascular pattern strongly resembles that observed for human ChP (Hudson, 1960). As such, it provides an anatomical roadmap that allows specific subregions of the lateral ventricle ChP to be identified and analyzed across mice within the same study, across studies from different labs, and across species.

ChP explants were stabilized for acute *in vitro* imaging (**Figure 1E**). To visualize calcium activity in epithelial cells, we gently dissected and stabilized the entire LV ChP from one hemisphere. We expressed the calcium reporter GCaMP6f (using *Ai95D* mice; Madisen et al., 2015) in ChP epithelial cells (using *FoxJ1-Cre* mice that selectively target this cell population) (**Figure 1F**) (Lun et al., 2015a; Zhang et al., 2007). Using epifluorescence imaging, we could visualize spontaneous calcium activity across thousands of epithelial cells simultaneously (**Figure 1F; Video S1**). We focused on a subregion and performed activity-based cell segregation (STAR Methods), resulting in time courses of spontaneous activity in individual epithelial cells (**Figures 1F-1K; Video S1**). Most epithelial cells showed large, transient

elevations in calcium activity lasting several seconds (**Figures 1K and 1L**). Such events were not synchronized across cells (**Figure 1M**). These findings suggest baseline regulation of calcium levels and calcium-dependent signal transduction in ChP epithelial cells.

Activation of serotonin receptors stimulates secretion via VAMP3-mediated exocytosis

Elevated calcium regulates many cellular processes including gene transcription and secretion in other body epithelia such as the salivary gland (Ambudkar, 2016). One factor previously shown to elevate calcium levels in ChP cell lines in culture is serotonin (5-HT, 5-hydroxytryptamine) (Esterle and Sanders-Bush, 1992; Sanders-Bush and Breeding, 1990). Metabolites of the 5-HT signaling pathway are present in the CSF (Toda et al., 2013). CSF-5-HT can originate from multiple sources, including direct release by dorsal raphe nucleus serotonergic neurons that course along the ventricles and in close proximity to the ChP (Narboux-Neme et al., 2008; Okaty et al., 2020; Tong et al., 2014), and via peripheral circulation, originating, for example, from 5-HT secretion in the gut (Stasi et al., 2019) or platelets (Cloutier et al., 2012). We found that 5-HT (Audhya et al., 2012; Toda et al., 2013) triggered coordinated waves of calcium activity that recruited increasing numbers of ChP epithelial cells across the explant with higher concentrations of 5-HT (**Figures 2A, 2B, and S2E; Video S2**).

The 5-HT_{2C} serotonin receptor (**Figure 2C**) (Lein et al., 2007), a Gq/G_{11}-coupled G-protein coupled receptor (GPCR), is the most highly expressed GPCR in ChP epithelial cells (Lun et al., 2015a). We found that subcutaneous (SC) injection of WAY-161503, a selective agonist of 5-HT_{2C} (Rosenzweig-Lipson et al., 2006), drove robust immediate early gene expression in ChP (**Figures 2D, S2A, and S2B**). Antibodies available for this receptor have typically shown low signal quality. Thus, we used genome editing to generate a *Htr2c*^{mRuby3}

mouse line in which the fluorescent protein mRuby3 was inserted at the C-terminus of 5-HT_{2C} **(Figures S2C and S2D)**. 5-HT_{2C}-mRuby3 was functional in these mice, as subcutaneous injection of WAY-161503 in *Htr2c*^{mRuby3} mice induced *c-fos* expression similar to that observed in wild type mice (**Figure 2D**; fold increase in *c-fos* mRNA expression in *Htr2c*^{mRuby3} mice receiving WAY-161503 [3 mg/kg] vs. vehicle: 80.6 ± 17.3, mean ± s.e.m., n = 4 heterozygous male mice; *Htr2c* expressed from X chromosome). Fluorescence of the mRuby3 tag revealed receptor localization throughout ChP epithelial cells, including at the apical and basal membranes (**Figure 2E**). This localization is consistent with the prediction that ChP epithelial cells can sense both central and peripheral sources of 5-HT (**Figure S1C**). Accordingly, using higher-magnification two-photon calcium imaging, we obtained similar patterns of activation of an increasing number of cells with increasing concentrations of the 5-HT_{2C} agonist, WAY-161503 (**Figures 2F and S2E; Video S3**).

Application of 5-HT to dissociated ChP cells in culture can increase the transfer of water and protein secretion (Conn and Sanders-Bush, 1986; Esterle and Sanders-Bush, 1992; Watson et al., 1995). Our expression analyses confirmed that the secretory machinery commonly required for calcium-dependent gene induction, protein secretion, vesicle trafficking/release machinery, and/or homologs of proteins from other epithelia are expressed in ChP epithelial cells (e.g. *Vamp3, Snap23, Stx12, Stxbp4*), implicating vesicular exocytosis as a mechanism of protein secretion (**Figures S2F-2SJ**) (Dani et al., 2019; Lun et al., 2015a). In EM images of ChP epithelial cells, a high density of vesicles was observed near the apical membrane (**Figure S2I**, black arrows). VAMP3 showed the highest gene expression amongst vesicle proteins in the ChP (**Figure S2G,** RNA-seq data from (Lun et al., 2015a)), and VAMP3 protein expression was confirmed by immunoblotting and immunostaining (**Figures S2H and S2J**). These data led us to

166 investigate activity-dependent and VAMP3-mediated ChP exocytosis. Specifically, we used
167 AAV-VAMP3-pHluorin (Urbina et al., 2018), a pH-sensitive variant of GFP, to visualize
168 individual secretory events. pHluorin fluoresces upon plasma membrane fusion, when the lower
169 pH (~5.6) inside intact exocytic vesicles changes to a pH of 7.4 upon exposure to the
170 extracellular environment. The fluorescence signal disappears following endocytosis and re-
171 acidification of the vesicles (Sankaranarayanan et al., 2000).

172 We first expressed VAMP3-pHluorin in the Z310 ChP epithelial cell line (Zheng and
173 Zhao, 2002). Using total internal reflection fluorescence (TIRF) microscopy, a method with high
174 signal-to-noise ratio, fast frame rate (2 frames/s), and narrow fluorescence excitation and
175 emission ranges, we could capture numerous spontaneous vesicle fusion events (**Figure S2K;**
176 **Video S4**). To evaluate ChP secretion in a more naturalistic setting, we transduced ChP *in vivo*
177 with AAV-VAMP3-pHluorin, dissected ChP explants, and investigated vesicle fusion events *in*
178 *vitro*. Due to the elaborate apical structure of ChP epithelial cells including multiple microvilli
179 and cilia (**Figure S2I**), these cells were not amenable to TIRF microscopy (axial resolution <100
180 nm) without compressing the cells against a coverglass – a procedure that could compromise
181 cellular integrity or induce cellular responses to mechanical distortion. Instead, we used Airyscan
182 confocal microscopy (ZEISS LSM880) that afforded comparable signal-to-noise ratio and frame
183 rates (1.59 frames/s). We observed spontaneous VAMP3-mediated exocytosis in individual
184 epithelial cells in whole ChP explants (**Video S5**). We extracted fluorescence time courses of the
185 localized secretion events following spatial filtering of each image (**Figure 2G**). We then defined
186 regions with co-active pixels and extracted time courses (**Figures 2G, 2H, and S2L**). Strikingly,
187 5-HT_{2C} activation by WAY-161503 (delivered at levels similar to those that drove calcium
188 activity in **Figure 2F**) drove an increase in the rate of VAMP3-mediated exocytosis (**Figures 2H**

189 **and S2L; Video S5**). Our data using live imaging at subcellular resolution demonstrate that 5-
190 HT stimulates ChP exocytosis via activation of 5-HT_{2C}. More generally, our findings validate a
191 platform for fluorescence imaging in ChP explants, enabling high-resolution studies of calcium
192 activation, secretion, and other processes.

193

194 ***In vivo*** **imaging of ChP in awake mice**

195 Virtually nothing is known about the activity of ChP cell types *in vivo.* We developed a
196 deep-brain cannula implantation strategy that enables acute and longitudinal imaging of the ChP
197 over weeks and months in awake mice. A cannula and glass window were surgically implanted
198 above the lateral ventricle (**Figures 3A-3D**), similar to our recent approach for imaging in visual
199 thalamus (Liang et al., 2018). At 2-3 weeks post-surgery, windows were typically translucent,
200 allowing brightfield imaging of ChP (**Figure 3E**).

201 Similar to brain surgery in the clinical setting, insertion of the imaging cannula is an
202 invasive procedure. We performed additional control experiments to determine the extent of the
203 injury response and to verify the health of the preparation following recovery from surgery at the
204 time of imaging. As anticipated, GFAP-positive astrocytes and *Cx3cr1*-positive immune cells
205 were enriched in cerebral cortical tissue adjacent to the cannula (**Figures S3A-S3G**). The density
206 of glial cells (GFAP-positive) and immune cells (*Cx3cr1*-positive) dropped to baseline levels by
207 ~100 μm from the edge of the cannula (**Figures S3A-S3G**). The ventricular lining of the lateral
208 ventricle below and lateral to the implant did not show accumulation of GFAP- or *Cx3cr1*-
209 positive cells, and retained characteristic S100β-positive ependymal cells (**Figure S3B**).
210 Importantly, immune cells from the ChP tissue located below the implant exhibited a ramified,
211 non-activated morphology with extended processes and a level of tiling of the ChP that was

212 indistinguishable from observations in contralateral ChP and in ChP from control mice that did
213 not undergo surgery (see **Figures 1A, 1B, 1C, S3H, and S3I**). Elevated CSF cytokine levels that
214 were evident in some mice one day following surgery also returned to undetectably low levels in
215 all mice by 3 weeks post-surgery (**Figure S3J**). These data demonstrate that, at the time that
216 imaging began several week post-surgery, our imaging preparation did not show signs of
217 persistent inflammation.

218 Epifluorescence images of lateral ventricle ChP from transgenic mice expressing
219 GCaMP6f in ChP epithelial cells (*FoxJ1-Cre::Ai95D*; **Figure 3F; Video S6**) demonstrated
220 consistently high image quality across mice. Notably, anatomical features of the ChP were stable
221 upon repeated imaging across weeks and months, with no evidence of substantial remodeling of
222 vasculature across imaging sessions beginning several weeks following surgery (**Figure 3G**).
223 While the location of the ChP in the lateral ventricle showed moderate mouse-to-mouse
224 variability following surgery (**Figure 3F**), identification of arterial and venous landmarks
225 allowed longitudinal imaging of a similar anatomical region of the ChP across mice, and within
226 the same mouse across sessions (**Figures 3 and S1B**).

227 To maximize spatial resolution and minimize bleaching during cellular imaging, we
228 performed two-photon imaging using a long working-distance, high numerical aperture objective
229 coupled to the imaging window (see STAR Methods). We targeted local regions of interest
230 within previously acquired epifluorescence images (**Figures 4A-4C**). In contrast to other brain
231 tissues that can be largely pressurized and stabilized for two-photon imaging (Goldey et al.,
232 2014; Liang et al., 2018), the ChP is only anchored at one edge near the base of the lateral
233 ventricle, and is otherwise suspended in CSF. Therefore, the ChP often exhibited large and non-
234 rigid motion in three dimensions during changes in behavior such as locomotion or adjustment of

235 body posture (**Video S6**). As described below, we used different imaging strategies and custom
236 registration algorithms to overcome these technical challenges.

237 First, video-rate two-photon imaging of a single plane allowed precise and high-speed
238 tracking of small numbers of cells following in-plane alignment, particularly during periods of
239 minimal brain motion while the mouse was stationary. For these analyses, occasional large tissue
240 movement could be stabilized or omitted from further analyses. Second, for longitudinal tracking
241 across hours, for which larger non-rigid motion and drift of the tissue out-of-plane were often
242 evident, we instead used a volumetric imaging strategy (0.25-0.5 volumes/s, 31-62
243 planes/volume, volume dimensions: 170 x 170 x 350 μm^3 or 355 x 230 x 100 μm^3; see STAR
244 Methods). This approach was important for achieving stable cell tracking following non-rigid
245 alignment in three dimensions (see **Figure 5**, below).

246

247 **Imaging calcium activity and apocrine secretion in ChP epithelial cells *in vivo***

248 We imaged ChP epithelial cell calcium activity using a transgenic mouse expressing
249 GCaMP6f, which provided similar expression levels across cells and stable expression across
250 days (**Figures 4A-4C**; see also **Figure 1F**). We first performed single-plane two-photon calcium
251 imaging (**Figure 4D)**. High-speed imaging (33-41 frames/s) revealed spontaneous subcellular
252 calcium events lasting ~200 ms (**Figure 4G; Videos S7-S8**). To quantify this observation, we
253 manually outlined the borders and nuclei of individual cells (**Figures 4D-4F**). A typical
254 subcellular event from one example cell is shown in **Figure 4G**. We segmented each cell into 12
255 radial sectors extending from the center of the nucleus (**Figure 4E,** bottom), and "unwrapped"
256 the sectors to create a kymograph of averaged subcellular activity across frames (**Figure 4H**). A
257 maximum intensity projection across sectors revealed large subcellular events (**Figure 4I**) of a

consistent duration and characteristic exponential decay (**Figure 4J**). The consistent dynamics and correlated changes across nearby pixels for this and other cells (**Figure S4**) further suggested that these events were not due to photon noise or brain motion. In contrast to maximum-intensity projections across sectors, median projections showed no significant fluctuations (**Figures 4K, S4A, and S4B**), consistent with the subcellular nature of these events.

Our earlier findings demonstrated that application of 5-HT_{2C} agonist WAY-161503 evoked robust calcium responses in ChP epithelial cells *in vitro* and induced immediate early gene expression following peripheral injection *in vivo* (**Figures 2D, 2F, S2A, S2B, and S2E; Video S3**). Further, signatures of apocrine section (**Figures 4M and 4N; Video S9**) have previously been reported to occur in ChP *ex vivo* (Agnew et al., 1980; Farkaš, 2015; Gudeman et al., 1989). We therefore sought to define the dynamics of ChP calcium activity and apocrine secretion upon WAY-161503 delivery *in vivo*. To obtain stable estimates of calcium transients across tens of minutes (see above), we used volumetric imaging (0.32 volumes/s, 93 planes/volume, 3.8 μm spacing between planes). Subcutaneous injection of WAY-161503 resulted in robust increases in calcium activity that progressed along the epithelium over tens of minutes (**Figure 4L; Video S9**). The large differences in timing of activation of various cells may relate to cell-to-cell differences in 5-HT_{2C} expression (**Figure 2E**), to slow changes in the concentration of WAY-161503, or to sequential sensing of signals release from activated neighboring cells. Cellular increases in calcium activity culminated in apocrine secretion, reflected by a release of cytoplasmic protrusions from the apical surface of the cell and cellular release of cytoplasmic contents directly into the CSF (**Figures 4L-4N; Video S10**). The basal portion of the cells including the nucleus remained intact. Taken together, these findings highlight novel *in vitro* and *in vivo* approaches to test and visualize calcium activity and distinct

281 modes of exocrine signaling by ChP epithelial cells. Further, these data establish a platform for
282 testing how exogenous signals such as serotonin can stimulate calcium activation, gene
283 transcription, and exocrine secretion.
284
285 **ChP immune cells at baseline and in response to local or peripheral stimulation**
286 The ChP is not only important for secretion of water and proteins into the CSF, but is also
287 an essential barrier that protects the brain from harmful blood-borne factors (Ghersi-Egea et al.,
288 2018; Saunders et al., 2018) and is implicated as a site of immune cell entry into the brain (Fame
289 and Lehtinen, 2020; Ghersi-Egea et al., 2018; Reboldi et al., 2009; Schwartz and Baruch, 2014;
290 Shechter et al., 2013). However, the *in vivo* functions of ChP immune cells in physiological or
291 pathological conditions remain largely unexplored (Kierdorf et al., 2019). Thus, we investigated
292 ChP immune cells under homeostatic, immune-challenged, and injury conditions.
293 We repeated the surgical approach described above in transgenic mice expressing GFP in
294 *Cx3cr1*-positive immune cells (Jung et al., 2000). Following surgical recovery, we performed
295 intraperitoneal (IP) injection of Texas Red-conjugated dextrans that rapidly filled the major
296 vessels and fine capillary networks of the ChP. These large dextrans (70 kDa) did not
297 immediately leak into the ChP stromal space. We then performed two-color imaging of ChP
298 immune cells and vasculature (**Figure 5A**), focusing on regions of ChP that were oriented
299 parallel to the imaging plane, and thus amenable to time-lapse volumetric imaging across the
300 thickness of the tissue (**Video S11**).
301 For tracking of fine immune cell processes across seconds, minutes and hours in awake
302 mice, it was critical to develop a procedure for accurate alignment of the 3D imaging volumes
303 (see **Figure 5B** and legend). It was useful to estimate shifts in ChP using the stable, bright red

304 dextran signal, and then apply these shifts to both the imaged vasculature (red) and immune cells
305 (green). Given that the individual frames were acquired at 15.5 frames/s, there was minimal
306 within-plane non-rigid motion. However, brain motion could result in X and Y shifts in
307 successive imaging planes within a volume (**Video S12**). Thus, alignment of each Z-plane to a
308 reference plane within each volume was important (**Figures 5C and 5D**). We then performed
309 rigid-body 3D alignment. Following these corrections, images of static objects (e.g. vasculature)
310 could be effectively stabilized (**Figures 5E and 5F**). As a final step, we calculated the mean
311 intensity across Z-planes for each volume and ran a second translational alignment. Across all 20
312 sessions from 13 mice, estimated intra-volume and inter-volume shifts in X, Y and Z could be
313 quite large, reflecting ChP suspension in CSF (**Figures 5G-5J**).

314 We observed substantial exploratory movements of ChP immune cell bodies and/or distal
315 processes. In each of 26 fields of view from 14 mice, we observed large numbers of GFP-
316 positive immune cells. Some of the cells were located within the ChP stromal space, while others
317 were located on the apical surface of the ChP, in contact with lateral ventricle CSF (i.e.,
318 epiplexus or Kolmer cells) (**Figures 6A-6G**). Epiplexus cell bodies often exhibited substantial
319 mobility. For example, the cell in **Video S13** (*top left*) traveled 210 μm in 1 hour. Some
320 epiplexus cell bodies moved at a constant rate, while others displayed saltatory movements
321 (**Figure 6D; Video S13**). In contrast, the majority of GFP-positive immune cells located within
322 the stromal space showed minimal cell body mobility. However, these cells possessed highly
323 dynamic processes that extended and contracted (**Figures 6E-6G; Video S13**), similar to
324 microglia in other brain areas (Hierro-Bujalance et al., 2018). These processes appeared to serve
325 a surveillance function, as they frequently contacted vessels within the stromal space, and

retracted upon contact with other processes from the same or neighboring immune cells (**Figures 6E-6G; Video S13**).

These surveillance-like behaviors were reminiscent of immune cells in other parts of the brain that play key roles in sensing environmental perturbations and protecting against injury (Hickman et al., 2018; Kierdorf et al., 2019; Li and Barres, 2018). Indeed, we found that immune cells in the ChP appear to partake in similar functions. First, we noted that the fluorescent dextrans used to label vasculature were cleared from circulation over several days. In these experiments, ChP immune cells in the stromal space, but not epiplexus cells, took up fluorescent dextrans 30 minutes following injection (**Figures 6H and 6I; Videos S14 and S15**), and dextran-labeled punctae could be observed even 26 days following injection (**Figures S5A-S5C**). These data demonstrate that ChP immune cells participate in uptake of foreign material from the peripheral circulation, consistent with the known housekeeping functions of immune cells in other parts of the body and brain.

The ChP contributes to blood-brain communication during peripheral inflammation (Balusu et al., 2016b), and the effects of immune challenges on the ChP have been implicated in several neurologic conditions. For example, genetic markers of immune function and inflammation are upregulated in ChP of schizophrenia patients (Kim et al., 2016). Thus, we next considered the effects of peripheral administration of the bacterial endotoxin lipopolysaccharide (LPS), which induces inflammatory responses in mouse ChP (Balusu et al., 2016b; Marques et al., 2009), on ChP immune cell morphology *ex vivo* and *in vivo.* As expected, LPS induced an inflammatory cytokine response in serum and CSF (**Figures 7A and S6A**). Using immunohistochemistry, we found that while peripheral LPS administration did not affect tiling of immune cells across the ChP (**Figures 1A-1C, S3H, and S3I**), it triggered a marked

repositioning of GFP-positive immune cell bodies and processes to regions surrounding the vasculature within the ChP (**Figures 7B, 7C, and S6B**).

To define the morphological dynamics of individual immune cells in response to LPS, we performed *in vivo* two-photon imaging during peripheral delivery of LPS. Many GFP-positive ChP immune cell bodies and processes that were initially located distal to vessels prior to LPS moved towards and spread along nearby vessels within ~45-60 minutes of LPS delivery (**Figure 7D; Video S16**). Using a custom algorithm to segment vasculature and define periluminal regions (**Figures 7E, 7F, and S6C**; STAR Methods), we confirmed that immune cell fluorescence increased in periluminal regions (**Figure 7F**). Not all *Cx3cr1*-expressing cells responded to LPS, consistent with the multiplicity of *Cx3cr1*-expressing ChP immune cell types that likely exhibit distinct responses to peripheral stimuli (Dani et al., 2019; Van Hove et al., 2019). This repositioning of ChP immune cells along the periluminal region may provide an extra layer of brain protection from harmful blood-borne signals during peripheral inflammation (Mottahedin et al., 2019).

In addition to the robust response of ChP immune cells following peripheral inflammation, we found that these cells often move towards sites of local injury. We induced a focal injury by high-power two-photon heating of a small area in the center of the field of view (89x57 μm^2, **Figure 7G**). This triggered rapid recruitment of immune cells to the injury site from nearby regions of the ChP. Immune cells initiated movement immediately following the laser injury, transitioned to an apparently more activated state (retracted processes, larger cell bodies), and continued moving until they stabilized in an aggregate surrounding the injury site (**Figure 7H; Video S17**). Across three mice, most but not all immune cells moved towards the injury site (**Figure 7I**). The majority of the cells that did move towards the injury site were confirmed to be

372 epiplexus cells (**Video S18**). Together, these findings reflect diverse contributions of different
373 types of resident ChP immune cells to host defense.

374

375 **DISCUSSION**

376 The scarcity of experimental tools for selectively targeting, monitoring, and manipulating
377 ChP cells has hindered progress in understanding this essential and distinct organ located deep
378 within the brain. Despite its principal roles in producing CSF, forming a brain barrier, and
379 secreting important health and growth promoting factors for the brain (Fame and Lehtinen, 2020;
380 Ghersi-Egea et al., 2018; Lun et al., 2015b; Saunders et al., 2018), remarkably little is known
381 regarding the functions of its cellular networks. Here, we developed imaging and analysis
382 approaches for monitoring and pharmacological manipulation of multiple ChP cell types in live
383 explants and in awake mice. Using a combination of epifluorescence, confocal, and two-photon
384 microscopy in ChP explants, we observed spontaneous calcium activity as well as spontaneous
385 exocytotic fusion events in individual epithelial cells. Both of these processes were enhanced by
386 application of agonists of the 5-HT_{2C} receptor, which is highly expressed in ChP epithelial cells.
387 Epifluorescence and two-photon microscopy in awake mice revealed subcellular spontaneous
388 calcium activity and 5-HT_{2C} agonist-evoked calcium activity and apocrine-type exocrine release.
389 By developing tools for volumetric, multi-color two-photon imaging of vasculature and immune
390 cells within and on the surface of the ChP *in vivo*, we uncovered spontaneous surveillance
391 behaviors of immune cells as well as profound immune cell activation and translocation
392 following peripheral or local perturbations. We hope this ChP imaging toolkit will accelerate the
393 pace of discoveries regarding the diverse functions of this vital deep brain tissue.

394

Imaging the ChP *in vitro* and *in vivo*

We hope these methods for imaging ChP explants can be of broad utility, as this approach is relatively simple and inexpensive, and allows tracking of tissue prior to and following controlled delivery of multiple drugs to the apical surface of the ChP. Our description of vascular landmarks should also improve repeatability within and across studies. The lateral ventricle ChP tissue is thin and delicate, and not entirely flat (albeit much flatter than third and fourth ventricle ChP). Thus, in order to obtain high-quality data, it was important to carefully extract the explant, stably mount it, and adjust fluid flow and osmolarity to avoid undue stretch/pressure (**Figure S1A**).

In vivo methods enabled monitoring of ChP in a largely natural environment during systemic delivery of drugs or perturbations (**Figures 4, 6, and 7**). While *in vivo* imaging using a cannula has been demonstrated in many deep brain areas (e.g., Dombeck et al., 2010; Liang et al., 2018), motion of ChP tissue posed a particularly challenging problem, as the ChP is anchored at the ventromedial aspect of the lateral ventricle, far from the dorsal ChP regions that we imaged. This likely contributed to substantial non-rigid motion in three dimensions beyond what is observed in other brain tissues that are pressurized and anchored by the imaging window. Thus, while our use of a treadmill to minimize head torque applied by the limbs likely reduced motion artifacts to some extent (Dombeck et al., 2007), it was critical to additionally use several methods for 2D and non-rigid 3D co-registration of imaging datasets in order to attain subcellular resolution (**Figure 5**). Another option to reduce coupling of body and brain motion could be to anesthetize mice prior to imaging. While this may be particularly useful for structural imaging studies, anesthesia could significantly alter the functional properties of the ChP.

We did not observe sustained inflammation of ChP for time points at which imaging was performed, several weeks following implantation (**Figure S3**). Intracranial pressure also normalized to baseline levels following this recovery period (data not shown). This recovery period also improved imaging clarity in comparison to acute imaging immediately following surgery (not shown), consistent with deep imaging in other brain regions (Goldey et al., 2014; Liang et al., 2018). Nevertheless, additional improvements to our approach could further minimize the invasive nature of the cannula implant. For example, with improved red and infrared fluorescent indicators, window implants for two- and three-photon imaging of ChP can be placed well above the dorsal surface of the lateral ventricle (e.g. Wang et al., 2018; Weisenburger et al., 2019). Alternatively, lower-profile GRIN lenses may be used for intraventricular imaging, albeit with a much smaller field of view and range of imaging depths.

Spontaneous and evoked calcium activity and vesicle fusion in ChP

We observed diverse rates of spontaneous calcium activity and diverse thresholds for evoked activity across nearby cells. These differences may relate to differences in activity states or to subtypes of epithelial cells. In future, such functional characterizations of epithelial cells can be merged with single-cell transcriptomics (Dani et al., 2019) to better understand potential divisions of labor across cells.

Spontaneous calcium transients were restricted to subregions of a cell. Future studies can assess whether these subcellular events relate to the subcellular vesicle fusion events we observed in explants, or to activation of a single protrusion among the many protrusions on the apical surface of each epithelial cell (evident in EM images in **Figure S2I**). These events were

particularly fast (~200 ms) when measured *in vivo*, possibly due to calcium imaging at warmer ambient temperatures *in vivo* vs. *in vitro.*

Application of a 5-HT_{2C} receptor agonist drove strong increases in calcium activity and increased rates of vesicular fusion. This calcium sensitivity of epithelial tissue to serotonin and associated agonists is consistent with previous reports using cultured, dissociated ChP cells (Watson et al., 1995). Higher concentrations of 5-HT_{2C} agonist evoked large, apocrine-type secretory events (**Figures 4L-4N; Video S9 and S10**) that have been reported in ChP and other epithelia including sweat and mammary glands (Farkaš, 2015). While these secretory events involve massive release of internal contents from an epithelial cell, they do not imply that cell health is compromised. Rather, this process may represent an efficient and rapid means for activity-dependent secretion of large amounts of cargo in response to an external stimulus, possibly in conjunction with other rapid changes (e.g. rapid activation of water and ion channels). Our studies set the stage for more in-depth investigations of how the ChP dynamically regulates the molecular composition of the CSF that bathes the CNS.

Immune surveillance at the ChP

Immune cells have been proposed to enter the brain via the ChP (Ghersi-Egea et al., 2018; Reboldi et al., 2009; Schwartz and Baruch, 2014; Shechter et al., 2013), but little is known about the functions of resident ChP immune cells during baseline conditions or in response to peripheral immune challenge or local injury. Tracking of *Cx3cr1*-expressing ChP immune cells together with vascular labeling *in vivo* revealed vascular surveillance by stromal immune cell processes, while cell bodies remained largely immobile. This surveillance points to active maintenance and phagocytic roles at the blood-CSF barrier. Notably, we found that these stromal

462 immune cells still contained 70 kDa dextrans *weeks* after IP injection. In contrast, epiplexus cells
463 on the apical surface of the ChP showed much greater cell body mobility but did not take up
464 dextrans.

465 ChP immune cells also responded to systemic LPS delivery by spreading their cell bodies
466 and processes along the periluminal region near blood vessels, a finding confirmed using
467 immunohistochemistry. This cellular response may reflect a means of protection against
468 peripheral insults, and differs from that of cortical microglia, which retract their processes and
469 adopt an amoeboid "activated" shape during inflammation (Pozner et al., 2015). Without access
470 to the time-lapse *in vivo* imaging, it would not have been possible to determine whether the same
471 local immune cells change their morphology and location or whether new immune cells had
472 entered the same region of ChP. Indeed, despite previous reports that immune cells cross at the
473 ChP (Ghersi-Egea et al., 2018; Reboldi et al., 2009; Schwartz and Baruch, 2014; Shechter et al.,
474 2013), our imaging sessions did not reveal arrival or departure of new immune cells from either
475 the CSF or the vasculature during baseline conditions or following LPS. Future studies should
476 examine deeper regions of the lateral ventricle across a broader range of conditions to more fully
477 assess potential subregions that mediate transit of immune cells to and from the brain.

478 We also noted rapid mobilization of nearby immune cells following deliberate heating of
479 a focal region of the field of view using transient, high-magnification and high-power two-
480 photon imaging. Many of these cells were epiplexus cells, which acted as "first responders" by
481 accumulating at the injury site. This behavior is strikingly different from that of *Cx3cr1*-positive
482 microglia in cortex and other brain regions (Davalos et al., 2005; Pozner et al., 2015), which
483 extend their processes towards a laser-induced lesion to contain the injury while their cell bodies

484 remain stationary (Davalos et al., 2005). Our findings can inform surgical procedures involving
485 focal heating of ChP, such as during cauterization of ChP to treat hydrocephalus (Warf, 2005).

486 In future, it should be possible to use the *in vivo* imaging approach described here to
487 assess the role of changes in calcium and other intracellular signals in immune cells, epithelial
488 cells and other stromal cell types in the ChP during these and other immune challenges and brain
489 injuries. A better understanding of the dynamic roles of multiple ChP cell types in various barrier
490 functions in the intact brain should spark new ideas for penetrating this barrier for drug delivery
491 to the brain, as well as for fortifying this barrier across the lifespan. More generally, given that
492 repeated *in vivo* access and chronic imaging may be more amenable in the ChP than in most
493 other body epithelia other than skin epithelium (Mesa et al., 2015; Rompolas et al., 2016), this
494 platform may provide a unique window into the general functions of barrier epithelia in their
495 natural environments.

496

497 **ACKNOWLEDGEMENTS**

498 We thank members of the Lehtinen, Andermann, and Moore labs for helpful discussions; A.
499 Lutas, K. Fernando, S. Marsh, M. Webb, C. Chen, O. Alturkistani, and the IDDRC Imaging Core
500 for advice and technical assistance; M. Bhaumik, BCH Genome Editing Core, G. Marsischky –
501 *Htr2c*^{mRuby3} design; M. Ericsson, HMS EM Facility; W.H. Fowle, NEU EM Facility, C. Wu at
502 the BCH Viral Core; S. Gupton for VAMP3 expression vector; J. Zhang for Z310 cells. This
503 work was supported by: NSF Graduate Research Fellowship (F.B.S.); Glenn/AFAR Postdoctoral
504 Fellowship, and Reagan Sloane Shanley Research Internship (N.D.); William Randolph Hearst
505 Fellowship (N.D. and J.C.); NIH T32 HL110852 (J.C. and R.M.F.); OFD/BTREC/CTREC
506 Faculty Development Fellowship Award (R.M.F.); NIH NIAID R01-AI130591 (T.K. and K.H.);

NHLBI R35-HL145242, (M.J.H.); GM075252 (T.K.); gift from the Korn family and NSF NeuroNex 1707352 (C.I.M.); David Mahoney Neuroimaging Grant Program – Dana Foundation, NIH DP2 DK105570, DP1 AT010971, R01 DK109930, R21 EY03043-02, McKnight Foundation, Pew Foundation, Smith Family Foundation, Klarman Family Foundation, and the American Federation for Aging Research (M.L.A.); Pediatric Hydrocephalus Foundation, Tommy Fuss Center Innovation Grant, Simons Foundation (SFARI [award #610670]), Harvard Brain Science Initiative Bipolar Disorder Seed Grant, NIH R01 NS088566 (M.K.L.), Human Frontier Science Program #RGP0063/2018 (C.W. and M.K.L.); NIH RF1DA048790 (C.I.M. and M.K.L.); the New York Stem Cell Foundation (NYSCF) grants #NYSCF-R-NI39 (C.W.) and #NYSCF-R-NI38 (M.K.L.); BCH IDDRC 1U54HD090255. C.W. and M.K.L. are New York Stem Cell Foundation – Robertson Investigators. The content is solely the responsibility of the authors and does not necessarily represent the official views of the National Institutes of Health.

AUTHOR CONTRIBUTIONS

F.B.S., N.D., M.L.A., C.I.M., and M.K.L. designed the study; N.D. and F.B.S. developed whole tissue explants and imaging protocols; C.D. and M.L.A. developed the *in vivo* 2-photon calcium imaging protocol; F.B.S. performed all computational analyses of all imaging data with advice from M.L.A.; J.C. helped generate *Htr2c*^{mRuby3} mice; F.B.S., J.C., and M.L.S. analyzed peripheral activation of immune cells; H.X. analyzed secretory pathways, and developed the vesicle imaging assay with assistance from C.W., K.H., and T.K.; J.H. developed immediate early gene assays; G.J.G. developed and T.K., E.J., E.K., V.I.F., and C.S. refined the imaging cannula approach; J.C. and R.M.F. analyzed CSF cytokines; Y.Z. and M.J.H. shared *FoxJ1-Cre* mice; F.B.S., M.L.A., and M.K.L. wrote the manuscript.

DECLARATION OF INTERESTS

The authors declare no competing interests.

FIGURE LEGENDS

Figure 1. Isolation, immunostaining, and calcium imaging of lateral ventricle ChP explants. **(A)** *Left*: large leaf of LV ChP from a *Cx3cr1*$^{+/GFP}$ mouse immunostained with anti-GFP (green, immune cells) and PECAM (red, vasculature). Scale, 500 μm. *Right*: zoom-in of small dashed box. Scale, 100 μm. *Cx3cr1*$^{+/GFP}$ cells tile the ChP (confirmed in 8 other mice). **(B)** Positions of 1781 *Cx3cr1*$^{+/GFP}$ cells from **A**. **(C)** Cumulative distribution of nearest-neighbor distances of each *Cx3cr1*$^{+/GFP}$ cell. Immune cells showed regular spacing (~30 μm) relative to random Poisson spacing (red trace; gray envelope: 1% acceptance interval). **(D)** PECAM (red) and ACTA2 (green) immunostains demarcate stereotyped LV ChP regions (confirmed in 3 other mice). Blue arrowheads: veins. Scale, 500 μm. **(E)** Light path and setup for imaging LV ChP. **(F)** Epifluorescence image containing a *FoxJ1-Cre::Ai95D* LV ChP explant expressing GCaMP6f in multiciliated ChP epithelial cells. Cells near stabilizing glue attachments at explant borders (asterisks) showed elevated GCaMP6f fluorescence (indicating unhealthy cells) and were

553 excluded from subsequent analyses. Scale, 1 mm. **(G)** Zoom-in of 122 epithelial cells (dashed
554 box in **F**). Scale, 50 μm. **(H)** Cell masks (see STAR Methods). **(I)** Twenty labeled cells
555 corresponding to traces in **K**. **(J)** Pink: traces surrounding each calcium transient with a
556 fractional change in fluorescence, $\Delta F/F > 5\sigma$ (235 events across 122 cells from **H**). Red: mean
557 calcium transient across traces. **(K)** Five-minute time courses from cells in **I**. **(L)** 76% (93/122)
558 of cells in **H** exhibited calcium events. **(M)** Average of all cross-correlations between binarized
559 event time courses of all pairs of cells from **H** (computed at delays from -5 to +5 s),
560 demonstrating that spontaneous events were uncorrelated across cells. We observed qualitatively
561 similar results as in **G**-**M** in 25 other mice, not shown. See also **Figure S1; Video S1**.
562
563 **Figure 2. Evoked calcium activity and exocrine secretion in ChP epithelial cells. (A)**
564 Epifluorescence calcium imaging of ChP epithelial cells from *FoxJ1-Cre::Ai95D* LV ChP
565 explant. Mean baseline fluorescence (*left*) and changes in fluorescence from baseline in response
566 to 0, 5, 50, and 500 nM 5-HT. Scale, 100 μm. **(B)** Time course of changes from baseline,
567 averaged across the explant. Responses to at least one dose of 5-HT were observed in 18/19
568 mice, and to all three doses in 10/19 mice, not shown. **(C)** *Htr2c* expression in LV ChP (from
569 Allen Brain Atlas, Lein et al., 2007). Scale, 500 μm. **(D)** *c-fos* induction following injection of 5-
570 HT_{2C} agonist WAY-161503 (****$p < 0.0001$, t-test, saline vs. 3 mg/kg SC; left to right: n =
571 8,8,2,2,2). **(E)** $Htr2c^{mRuby3}$ LV ChP labels 5-HT_{2C} receptors in epithelial cells. Axial (*left*) and
572 side-on (*right;* from dashed box at left) maximum projections show preferential apical (apposed
573 to the CSF) vs. basal (closer to vessels) localization. Scale, 10 μm. **(F)** Two-photon imaging of
574 *FoxJ1-Cre::Ai95D* explants. Higher concentrations of WAY-161503 activated more cells (green
575 arrowheads), and cells activated at lower concentrations are not reactivated later. Responses were

observed in 7/7 mice, and to each dose in 5/7 mice (not shown). Scale, 10 μm. **(G)** Confocal imaging of vesicle release from an example LV ChP epithelial cell following viral expression of VAMP3-pHluorin. *Top left*: maximum intensity projection across baseline period shows fluorescent vesicle release (white punctae). *Bottom left*: similar projection following Hessian-based filtering. *Middle panels*: same as left but following application of WAY-161503 (500 nM). *Right*: vesicle release event masks segmented from the filtered movie. Scale, 5 μm. **(H)** Cumulative number of VAMP3-pHluorin vesicle release events following application of WAY-161503 (red) or aCSF (blue). See also **Figure S2; Videos S2-S5**.

Figure 3. Imaging lateral ventricle ChP in awake mice. (A,B) Schematic of cannula (gray cylinder) with glass bottom, implanted above the LV ChP (green). **(C)** Headpost placement. **(D)** Head-fixed mouse on a trackball. An immersion well attached to the headpost allowed imaging via a high numerical aperture objective. **(E)** Brightfield image of ChP through the cannula, 27 days post-surgery. Dotted line outlines ChP. **(F)** Epifluorescence images of ChP (arrowheads) from *FoxJ1-Cre::Ai95D* mice, 42-56 days after surgery. Scale, 1 mm. **(G)** Tracking the same ChP (arrowheads) via a clear window across many days following surgery (similar results observed in 9 other mice, not shown). Scale, 1 mm. See also **Figure S3; Video S6.**

Figure 4. Two-photon calcium imaging of epithelial cells in awake mice. (A) Epifluorescence image of GCaMP6f-expressing ChP epithelial cells (diagonal vascularized sheet; *FoxJ1-Cre::Ai95D* mouse). Scale, 1 mm. **(B)** Zoomed-in image (dashed red square in **A**). Scale, 100 μm. **(C)** Maximum projection of two-photon imaging volume encompassing the ChP region in

598 **B**. Scale, 100 μm. **(D)** Average of images at a single plane. Scale, 50 μm. **(E)** Individual
599 epithelial cell (red square in **D**), annotation of cell outline and nucleus, and division into 12
600 sectors. **(F)** Annotation of all cell outlines and nuclei in **D**. **(G)** Time-lapse of a single subcellular
601 calcium event. **(H)** Kymograph of activity across all 12 sectors of cell in **E**,**G**. Red arrowhead:
602 event from **G**. **(I)** Time course of brightest-sector activity (black, maximum across sectors in **H**)
603 and median activity (red). Asterisks: peaks of subcellular events exceeding 3 std (dashed blue
604 line) above a running mean. **(J** and **K)** Brightest-sector (**J**) and median-sector (**K**) activity
605 surrounding peak (t=0) of all events for cell in **E**. Thicker lines: mean traces. Similar results were
606 observed in 3 other mice, not shown. **(L)** Images of cross-sections of two sheets of GCaMP6-
607 expressing epithelial cells separated by stromal space, beginning 25 min after injection of WAY-
608 161503 (3 mg/kg, SC; similar results observed in 2 other mice, not shown). Scale, 50 μm. **(M)**
609 Zoom-in of a single epithelial cell reveals release of subcellular plumes (arrowheads) of
610 intracellular contents including GCaMP6f into CSF. The basal side of the epithelium remained
611 intact, consistent with apocrine secretion. Scale, 10 μm. Similar events were observed in a
612 second mouse, not shown. See also **Figure S4**; **Videos S7-S10**. **(N)** Scanning EM of ChP, 15
613 min following WAY-161403 (3 mg/kg, SC) reveals apocrine blebs (arrowheads). Scale, 5 μm.

614

615 **Figure 5. 3D imaging and registration of ChP in awake mice. (A)** Maximum projections
616 across a time-averaged two-photon imaging volume of *Cx3cr1*$^{+/GFP}$ immune cells (green) and
617 Texas Red dextran-labeled vasculature (red, IP injection). Projections from two mice are shown
618 (similar results in 13 other mice, not shown). Scale, 100 μm. **(B)** Registration algorithm (see
619 STAR Methods). Step 1: correct for depth-dependent magnification due to tunable lens. Step 2:
620 intra-volume alignment of each plane to its neighbor. Step 3: 3D translation of each volume to a

621 local target. Steps 4-5: Z-projection and X-Y alignment. **(C)** Mean Z-projection of a single
622 volume, before vs. after Step 2. Scale, 50 μm. **(D)** Estimated X and Y corrections for each plane
623 of volume in **C**. **(E)** Z-profile time lapse of vasculature, before and after 3D registration.
624 Columns: 600 volumes spanning ~63 min; rows: average fluorescence in the white box in **C** at
625 each Z plane. White trace: estimated Z correction. **(F)** Index of motion artifact (sliding estimate
626 of [standard deviation]/[mean] vasculature fluorescence across volumes; see STAR Methods).
627 Registration reduced both large, transient motion artifacts (peaks in orange trace) and persistent,
628 higher-frequency motion (see **J**). **(G-I)** Cumulative distributions of X and Y displacements of
629 planes within each volume (**G**), and XY displacements (**H**) and Z displacements (**I**) across
630 consecutive volumes. Data in **G-J** from 20 sessions from 13 mice. **(J)** Mean motion artifact (see
631 **F**) per session, pre- vs. post-registration. **** $p < 0.0001$; paired t-test.

632

633 **Figure 6. ChP immune cells perform local surveillance and housekeeping *in vivo*.** **(A)** Cross-
634 section of ChP. Epiplexus immune cells (orange arrowhead) are located on apical (CSF-sensing)
635 surface of epithelium (green sheet). Stromal immune cells (blue arrowheads) are located in
636 stromal space between vasculature (red with purple endothelial cells) and epithelium. **(B)** *Top*:
637 axial mean projection of *Cx3cr1*$^{+/GFP}$ cells in LV ChP explant *ex vivo*. *Bottom*: side-on view.
638 Arrowheads indicate stromal (blue) and epiplexus (orange) immune cells. Scale, 100 μm. (**C**-**G**)
639 Similar to **C** but from *in vivo* two-photon imaging (see also **Videos S11 and S13**). Scale, 25 μm.
640 **(C)** Example epiplexus cells from 4 mice. Side-on views (bottom) indicate locations outside
641 vascular plane (likely outside the epithelium). **(D)** Example epiplexus cell pausing, then traveling
642 across the ChP surface (colored dots: cell location at 1-min intervals). **(E-G)** Example stromal
643 immune cells showed either stationary cell bodies with processes that survey nearby vessels (**E**-

644 **F**), and that retract following upon contacting a different immune cell (**F**), or, occasionally, cell
645 body movement constrained by surrounding vessels (**G**). **(H)** *Left, middle:* IP-injected red
646 dextran (70 kDa) fills the ChP vasculature. *Right:* 2 days later, dextran has leaked into stromal
647 space and accumulated within immune cells. Scale, 50 μm. (**I**) Snapshots of dextran punctae
648 accumulating within immune cell processes (arrowheads). See also **Figure S5; Video S14**.

649

650 **Figure 7. ChP immune cells respond to systemic and local insults. (A)** Higher CSF cytokine
651 levels 1-hr after IP injection of LPS vs. saline (mean ± s.e.m.; n = 3 samples, each consisting of
652 25 μl pooled across 3-6 mice; t-test, IL-1α, p = 0.0017; TNF-α, p = 0.0072; CCL2, p = 0.0260;
653 IL1β, p = 0.0451; IFN-β, p = 0.0212). **(B-D)** Following LPS, immune cells flatten along vessels**.**
654 **(B)** LV ChP explants from *Cx3cr1*$^{+/GFP}$ mice that received IP saline (*left*) or LPS (*middle*).
655 Segmentation of immune cells (right panel, green), and periluminal region surrounding
656 vasculature (blue; **Figures S6B** and **S6C**, STAR Methods) allowed assessment of overlap
657 (yellow). Scale, 50 μm. **(C)** Percentage of periluminal region occupied by immune cell processes
658 following IP saline (n = 15 explants, 9 mice) or LPS (n = 20 explants, 10 mice). ****p < 0.0001,
659 Welch's t-test. Mean ± s.e.m. **(D)** *In vivo* imaging of immune cells (green) and vasculature (red)
660 pre-LPS (left) and 3 hrs following IP LPS (right). Scale, 25 μm. Arrowheads: transitions of cell
661 bodies to splayed morphology (see **Video S16**). **(E)** Segmentation of periluminal region (STAR
662 Methods). **(F)** Fractional change in immune cell fluorescence (ΔF/F) in periluminal region across
663 4 hrs, relative to pre-LPS baseline (red line). **(G)** Schematic of focal injury via brief, high-power
664 focusing of a laser on a small region of ChP during *in vivo* imaging. **(H)** Maximum projections
665 of immune cells and vasculature before, 6 min after, and 1 hr after a local burn of the region
666 within the white box. At 6 min, dextran leaks out of damaged vessels (see **Video S17**). Immune

667 cell bodies then migrate to the injury site. Scale, 50 μm. **(I)** Average pre- and post-injury velocity
668 of immune cells towards (positive) or away from (negative) the injury site (n = 15 cells, 3 mice).
669 ** p = 0.0075, paired t-test.

670

671 **STAR METHODS**

672 ***RESOURCE AVAILABILITY***

673 **Lead Contact**

674 Further information and requests for resources and reagents should be directed to and will be
675 fulfilled by the Lead Contact, Maria Lehtinen (maria.lehtinen@childrens.harvard.edu).

676 **Materials Availability**

677 All unique/stable reagents generated in this study are available from the Lead Contact with a
678 completed Materials Transfer Agreement.

679 **Data and Code Availability**

680 The registration and vascular segmentation algorithms generated for this study are available at
681 https://github.com/LehtinenLab/Shipley2020. Original data is available from the corresponding
682 author upon request.

683

684 ***EXPERIMENTAL MODEL AND SUBJECT DETAILS***

685 All animal care and experimental procedures were approved by the Institutional Animal
686 Care and Use Committees of Beth Israel Deaconess Medical Center (Figures 3, 5-7), Boston
687 Children's Hospital (Figures 1-7), and Brown University (Figures 3, 4). Mouse lines used
688 include *FoxJ1-Cre* (Zhang et al., 2007), *Ai95D* (Jax# 024105; Madisen et al., 2015), $Cx_3cr_1^{+/GFP}$
689 (Jax# 005582; Jung et al., 2000), $Htr2C^{mRuby3}$, CD-1, and C57BL/6 (Figures 1, 2: male and

690 female mice; Figures 3-7 male mice). *Htr2C*^{mRuby3} mice were generated by the Gene
691 Manipulation & Genome Editing Core, IDDRC, BCH. Best-ranked sgRNAs near the targeting
692 region in *Htr2C* genome were picked (Doench et al., 2016) and synthesized (Alt-R® CRISPR-
693 Cas9 crRNA, Integrated DNA Technologies). Donor plasmid was custom made at GeneScript,
694 prepared with EndoFree Plasmid Maxi Kit (Qiagen). Alt-R® S.p. HiFi Cas9 Nuclease (Integrated
695 DNA Technologies) was used for the editing. A mixture of crRNA (0.61 μM), Cas9 protein (10
696 ng/μl), and donor (10ng/μl) was injected into 0.5 dpc embryos harvested from C57BL/6NHsd
697 (Envigo) mating pairs. Embryos that survived the injection were implanted into recipient
698 pseudopregnant females and allowed to reach term. Tail biopsies from pups were genotyped to
699 identify founders. The line was maintained in C57BL/6J.
700
701 ***DETAILED METHODS***
702 **ChP explant preparation**
703 Whole ChP from the lateral ventricle was harvested using #5 forceps and fine-dissection
704 scissors. To collect the LV ChP, the hindbrain was separated from the mid- and forebrain
705 structures using a scalpel, followed by a bilateral cut along the midline to separate the cortex into
706 two hemispheres. Each hemisphere was stabilized with forceps and a third of the rostral end was
707 cut off, the developing hippocampus was rolled out using the flat surface of a scalpel, and the
708 attached LV ChP was gently separated from the hippocampus/fornix using forceps.
709 LV ChP was transferred onto round coverslips (15 mm, Warner Instruments, Cat. 64-
710 0733) that had been prepared as follows: briefly, coverslips were lightly coated with Silicone
711 (Kwik-sil, World Precision Instruments, Item. 600022), and while wet (1xaCSF: 119 mM NaCl,
712 2.5 mM KCl, 26 mM $NaHCO_3$, 1 mM NaH_2PO_4, 11 mM glucose, with fresh 2.0 mM magnesium

713 chloride and 2.8 mM calcium chloride), a polycarbonate membrane (Whatman, Nucleopore, 13
714 mm wide, 8.0 µm pore size, Cat. 110414) was placed on the cover slip. Edges of the
715 polycarbonate membrane were attached to the coverslip using adhesive (3M, Vetbond). These
716 glass coverslips were kept at room temperature and allowed to cure. The ChP was flattened onto
717 the membrane and secured using 3M Vetbond. All samples were placed in a holding chamber
718 with continuously oxygenated (95% O_2 / 5% CO_2) 1xa CSF.
719
720 ***IN VITRO* EPITHELIAL CELL EXPERIMENTS**
721 ***In vitro* epifluorescence calcium imaging**
722 Epifluorescence calcium recordings were acquired from *FoxJ1-Cre::Ai95D* ChP explants (see
723 above) using a 4x, 0.28 NA objective (Olympus). A halogen lamp and FITC filter set (Olympus)
724 were used for excitation and emission filtering. Green fluorescence was collected using an
725 sCMOS camera (Hamamatsu). Images (2048 x 2048 pixels, 3.30 x 3.30 mm^2) were acquired at
726 10 frames/s using MicroManager (NIH).
727
728 **Segmentation of cell masks**
729 Epifluorescence calcium videos were cropped to a small region (161 x 161 μm^2) near the center
730 of the sample, for ease of processing. We obtained cell masks based on cell shape, as follows:
731 first, a mean image, *I*, was generated, and was locally contrast-normalized using:
732
$$I_n = \frac{I - G(I;\ \sigma = 3)}{\sqrt{G(I;\ \sigma = 3)}}$$

733 Where G is the 2D Gaussian operation. The normalized image was then binarized and watershed
734 to separate cells that were joined together. Objects smaller than 5 pixels were considered noise
735 and discarded. The convex hulls of remaining objects were used as cell masks. Neuropil masks

were estimated as the annulus spanning the region between the cell perimeter and the perimeter obtained after dilating the cell by 5 pixels.

Trace extraction

A raw trace, F(t), was extracted from each cell mask by calculating mean intensity across pixels in each mask, and for each movie frame. A neuropil activity trace, $F_{neuropil}(t)$, was calculated in the same way, using the corresponding neuropil mask. A neuropil-corrected signal, $F_{corrected}(t)$, was calculated by subtracting the neuropil trace from the raw trace, and adding back the mean of the signal:

$$F_{corrected} = F - F_{neuropil} + \bar{F}$$

The signal was further normalized by:

$$\Delta F/F = \frac{F_{corrected} - median(F_{corrected}, 500)}{median(F_{corrected}, 500)}$$

Where $median(F_{corrected}, 500)$ denotes a moving median filter with a window size of 500 frames (50 seconds) surrounding the time t.

Calcium events were defined as peaks in which $\Delta F/F > (5 \times std(\Delta F/F))$. Cells with traces that never exceeded this threshold were considered "inactive".

***In vitro* two-photon calcium imaging**

Two-photon microscopy was used to record calcium activity in explants in which ChP epithelial cells express GCaMP6f (in *FoxJ1-Cre::Ai95D* mice, using an Olympus MPE-RS two-photon microscope; 30.0 frames/s; 512x512 pixels/frame). All imaging was performed with a 25x, 1.0 NA objective (Olympus) at 4.5x digital zoom (~113 x 113 μm^2). Laser power measured below the objective at 940 nm was 55 mW using a Mai Tai DeepSee laser (Spectra-Physics). To

perform 3D recordings, the settings above were used in conjunction with a nPFocus250 piezo microscope stage (nPoint) moving axially in a sawtooth pattern. 3D volume recordings were acquired at ~0.25 Hz to capture baseline activity, during which time aCSF flowed through the perfusion chamber (Warner; performed at room temperature) containing the ChP explant. Subsequently, increasing concentrations of 5-HT or the 5-HT_{2C} selective agonist, WAY-161503 (Tocris), in aCSF were introduced for one minute per concentration, with ten minute aCSF washouts in between drug deliveries. To measure bulk tissue fluorescence, a mean volume projection along the axial (z) dimension was performed to flatten each 3D volume into a 2D image, resulting in a 2D video across time. Average fluorescence across the 10 minutes baseline period prior to the first drug delivery was used as a baseline image. A ΔF image stack was constructed by subtracting this baseline image from each frame in the video. A trace of ΔF activity was calculated as the mean pixel intensity of each frame of the image stack.

VAMP3-pHluorin imaging

Cultured cells: Z310 cells were cultured on glass coverslips and lipofectamine transfected with pAAV-VAMP3-pHluorin. After 3 days, the cells were imaged using TIRF microscopy (Cocucci et al., 2012) with a 100x objective (1.46 NA, Carl Zeiss) and a 2x magnification lens placed in front of the CCD camera (QuantEM, Photometrics). This arrangement provided a final pixel size of 80 nm. ChP explants: AAV2/5-VAMP3-pHluroin was injected *in utero* i.c.v. in E14.5 embryos. LV ChP explants were then harvested at P18-P24. Each ChP was attached directly onto an imaging dish using Vetbond and immersed with 1.8 ml of aCSF. WAY-161503 was added until the final bath concentration reached 500 nM. Individual epithelial cells from explants were

781 imaged using a ZEISS LSM880 Airyscan confocal microscope. The chamber, imaging dish
782 holder, and all buffers used were maintained at 37°C.

783 To detect secreted vesicles, each image frame was first smoothed with a two-pixel radius
784 Gaussian filter (160 nm). We then further filtered each image by calculating the determinate of
785 the Hessian matrix at every pixel, and this image stack was used to isolate VAMP3 fusion events
786 from cell background. Masks of regions involving a fusion event were obtained by PCA/ICA
787 segmentation (Mukamel et al., 2009). Fluorescent traces were extracted by averaging
788 fluorescence of all pixels within each mask. Each fluorescence trace was normalized to peak
789 fluorescence, and sorted the traces by the time at which this peak occurred, in order to generate a
790 heatmap of time courses of vesicle release events.

791

792 ***IN VIVO IMAGING EXPERIMENTS***

793 **Headpost and cranial window placement**

794 Mice used for *in vivo* two-photon imaging (8-20 weeks) were outfitted with a headpost
795 (titanium, 0.7 g, H.E. Parmer) and 3 mm cranial window using minor modifications of
796 techniques previously described (Goldey et al., 2014; Liang et al., 2018). Briefly, each cranial
797 window implant was first prepared by gluing a 3 mm x 2 mm (diameter x height) stainless steel
798 cylindrical cannula (MicroGroup) to a 3 mm diameter glass coverslip (Warner) using a UV-
799 cured optical adhesive (Norland, type 71). Approximately 3 hours prior to surgical implantation,
800 dexamethasone sodium phosphate (4 mg/ml, intramuscular) was administered in order to reduce
801 brain edema. Anesthesia was induced using isoflurane (1-3% in 100% O_2, with flow rate titrated
802 to a respiratory rate of 1 breath per minute). Using standard aseptic techniques and a
803 stereomicroscope, a 3-mm diameter craniotomy was performed over the left side of the skull,

804 centered using stereotactic coordinates (2.0 mm lateral and 0.2 mm posterior to Bregma). Next,
805 portions of neocortex, corpus callosum, and hippocampal tissue were carefully and slowly
806 aspirated to expose the lateral ventricle, with the specific purpose of preventing undue increase
807 in intracranial pressure. The ChP was visualized floating within the ventricle. Hemostasis was
808 achieved with copious irrigation using sterile phosphate-buffered saline and occasional use of
809 gelfoam. At this point, the cranial window implant was inserted through the craniotomy site and
810 lowered to a depth of approximately 2.0 mm below the skull where it pressed lightly on the
811 surface of the thalamus and preserved direct visualization of the intact ChP. The cannula was
812 temporarily affixed to the skull with Vetbond (3M) followed by a permanent seal with C&B
813 Metabond (Parkell). A custom two-pronged titanium headpost was then affixed to the skull and
814 again sealed with C&B Metabond (the headpost implantation can also be performed prior to the
815 craniotomy according to investigator preference).

816 To create a low-profile adaptor to accommodate the water-immersion objective and light
817 shielding, a custom 3D-printed imaging well (outer diameter of the base, inner diameter, height:
818 20 mm, 10 mm, 4 mm, or 7.5 mm, 5 mm, 1 mm) was then positioned around the cannula and
819 glued to the cement and headpost. Animals were given Meloxicam (0.5 mg/kg, s.c.), individually
820 housed, and allowed at least 2 weeks to recover before live imaging. The estimated success rate
821 in obtaining clear windows was ~80% for a trained surgeon. In the first post-operative week, the
822 mice were undisturbed and, during the second week, the mice were habituated to the imaging
823 environment. Each mouse was placed on a custom 3D-printed running wheel and the animal's
824 head was fixed using clamps (Thorlabs) that attach to each prong of the two-pronged titanium
825 headpost. The running wheel and associated flexible hinges were useful for decreasing brain
826 motion, by decreasing the degree to which hindlimb-related forces couple to brain motion.

During two-photon imaging sessions, the low-profile imaging well was covered with blackout fabric (Thorlabs).

IN VIVO EPITHELIAL CELL EXPERIMENTS

Epifluorescence imaging

To initially localize the ChP and assess stability and orientation of the ChP post-surgery, an epifluorescence video was recorded while scanning axially through the tissue. To account for lensing effects from changing z planes, planes were registered with scaled rotations to each other using the StackReg plugin in Fiji (NIH).

Two-photon imaging of spontaneous activity

To capture high-speed subcellular and cellular activity in epithelial cells *in vivo*, two-photon microscopy was used to record calcium activity in a ~25 cells. Imaging of GCaMP6f-expressing epithelial cells (in *FoxJ1-Cre::Ai95D* mice, see above) was performed using a resonant-scanning two-photon microscope (Olympus, 512x512 pixels/frame; Bruker, 490x372 pixels/frame). Spontaneous activity was recorded at a single imaging plane (Olympus, 30.0 frames/s; Bruker 41.5 frames/s). All imaging was performed with a 25x, 1.0 NA objective (Olympus) at 4.5x digital zoom (~113 x 113 μm^2). Laser power measured below the objective was 55 mW using a Mai Tai DeepSee laser at 940 nm (Newport Corp.).

Registration/preprocessing of spontaneous activity

To compensate for rapid ChP motion caused by mouse locomotion and changes in posture, each frame was registered to a target image created by the mean of the first 500 frames. Registration

was performed by cross-correlating the Fourier transform of each image with this target image (i.e. rigid-body translation correction; Guizar-Sicairos and Fienup, 2008).

Cellular and subcellular segmentation – spontaneous activity

After registration, a mean image across the entire recording was generated. Cell outlines and outlines of cell nuclei were manually drawn for each cell in the field of view (~20-40 cells). Cytoplasm masks were generated from the difference between cell mask and nucleus mask. Cytoplasm masks were subdivided into 12 radially symmetric subsections from the center of the nucleus. The neuropil area was an annulus surrounding the cell, calculated by dilating the cytoplasm masks by 10 pixels, and excluding pixels in the original cell mask from this dilated cell mask.

Subcellular trace extraction – spontaneous activity

First, the aligned video was down-sampled by a factor of 4. For each cell, the raw sector activity (i.e. a pie slice of the cell), $F_{raw}(\theta, t)$, was calculated as mean activity across pixels inside each of the cytoplasm sectors (θ) for every timepoint, *t*. Neuropil activity, $F_{neuropil}(t)$ was calculated as mean pixel activity in the neuropil mask defined above, at every timepoint, *t*. Neuropil activity was subtracted from raw activity to generate a neuropil-corrected time course:

$$F_{corrected}(\theta, t) = F_{raw}(\theta, t) - F_{neuropil}(t)$$

To normalize for different baseline section brightness, a rolling median of 6.67 s was subtracted from neuropil-subtracted signal:

$$\Delta F(\theta, t) = F_{corrected.}(\theta, t) - median_{\Delta t=6.67s}(F_{corrected}(\theta, t))$$

To find subcellular calcium events, the maximum signal across cell sectors was calculated, for each time t, by taking a maximum projection across sectors, and then subtracting the median across sectors:

$$F_{max}(t) = max_{\theta}(\Delta F(\theta, t))$$

$$\Delta F_{max}(t) = F_{max}(t) - median_t(F_{max}(t))$$

This approach generated a single trace of the largest fluorescence deviation from median fluorescence across cell sectors at every timepoint.

To identify subcellular events, a peak detector was applied to the above trace using a threshold based on the trace of median activity across sectors ('median trace', F_{med}). First, F_{med} was calculated as:

$$F_{med}(t) = median_{\theta}(\Delta F(\theta, t))$$

$$\Delta F_{med}(t) = F_{med}(t) - median_t(F_{med}(t))$$

Subcellular calcium events were defined as local peaks of epochs in which $\Delta F_{max} > (5 \times std(\Delta F_{med}(t)))$.

In vivo 3D imaging of epithelial cell responses to delivery of a serotonin agonist

To perform 3D recordings, the same imaging settings described above for spontaneous *in vivo* calcium imaging were used, but with the addition of a nPFocus250 piezo microscope stage (nPoint) that moved the imaging plane axially in a sawtooth pattern (scanning of 93 planes per volume across 350 μm of depth with a scan rate of frame rate of 30.0 frames/s, 512x512 pixels/frame, resulting in volume scanning of a 170x170x350 μm^3 volume at 0.32 volumes/s).

To register these volumes, we first averaged together every ten volumes in order to improve signal-to-noise ratio. Since the observed effects of WAY-161503 were slow and long

lasting, this approach did not overly compromise temporal resolution. Each plane of these average volumes was registered to the center z plane (middle plane) of the volume using the StackReg plugin in Fiji (NIH), creating a rectified volume. The maximum intensity projection of each of these rectified volumes were used to correct for inter-volume motion X-Y motion. Using the first volume as an anchor point, each volume was registered to the previous volume. X-Y plane transverse shifts were calculated by cross-correlating the Fourier transformations of the maximum intensity projection of a given volume and of the previous volume (Guizar-Sicairos and Fienup, 2008).

IN VIVO IMMUNE CELL EXPERIMENTS

Dextran injection

Mice received intraperitoneal injections of dextran conjugated with Texas Red (70 kDa 0.2 mg/gm IP). ThermoFisher Scientific), delivered 30 minutes before imaging. Presence of dextran in vasculature was confirmed by two-photon imaging.

Two-photon imaging

3D volume recording was necessary to robustly track the ChP across long timescales due to mouse motion, changes in posture, and occasional axial drift of ChP. Two-photon imaging of immune cells and vasculature was performed using a resonant-scanning two-photon microscope (experiments were performed on two different microscopes: Olympus; 12.8 frame/s; 512x512 pixels/frame; 0.16 volumes/s, 81 planes/volume; volume size: 254x254x400 μm^3. Neurolabware: 15.5 frames/s; 796x512 pixels/frame; 0.25-0.5 volumes/s, 31-62 planes/volumes; volume size: 355x230x100 μm^3). Volume scanning on the Olympus was achieved by using a piezo

microscope stage (nPFocus250). Volume scanning on the Neurolabware microscope was achieved using a tunable focus lens (Optotune). All imaging was performed with a 25x, 0.95 NA objective (Olympus) at 2x zoom (~254 x 254 μm^2 (Olympus), ~ 360 x 230 μm^2 (Neurolabware)). Laser power at 940-960 nm (Mai Tai DeepSee laser, Spectra Physics) measured below the objective was 30-40 mW. Immune cells were confirmed to be located within or on the outside of the ChP based on colocalization with the fluorescent dextran-labeled vasculature pattern.

3D registration

Due to the rapid motility of immune cells across seconds, 3D registration of individual volumes was necessary to properly account for ChP movement at these rapid timescales (see **Figure 5**). To account for optical deformation and warping caused by the focus-tunable lens, a counter-warping correction was calculated for each imaging session. The first 30 volumes were averaged together to create a mean distorted volume. The affine transformation was used to iteratively match each plane to its neighbor, beginning with the brightest plane of the volume and moving up and down until the ends of the volume. Since affine transformations are linear functions, the adjacent transformations could be combined by multiplication of the augmented transformation matrix to generate the warp-correction of every focus-tunable lens plane to the reference. These matrices are calculated using the MultiStackReg plugin in Fiji (NIH). Since these deformations were due to the optical system, not motion of the sample, these corrections were applied to every volume prior to subsequent motion correction (**Figure 5B**, “Step 1”). For the Olympus microscope that uses a piezo microscope stage to scan axially, there is no deformation, and this step is skipped.

940 Due to rapid motion caused by mouse movement, it was necessary to account for intra-
941 volume changes. Using the brightest plane as a stationary anchor plane, each plane was
942 registered to its neighbor, using Fourier cross-correlation to estimate the X and Y shifts. These
943 neighboring X and Y shifts were summed cumulatively so that each plane is aligned with the
944 anchor plane. (**Figure 5B**, "Step 2") (Guizar-Sicairos and Fienup, 2008).

945 After intra-volume alignment, reference volumes were generated by averaging every 20
946 volumes. To account for inter-volume lateral and axial shifts, each volume was then registered to
947 its respective reference volume by cross-correlating the 3D Fourier transformation of the two
948 volumes to find the X, Y, and Z shifts. Each reference volume was registered to the first
949 reference volume using the same method (**Figure 5B,** "Step 3").

950 Axial projections, such as mean, median, and maximum projections, were then performed
951 (**Figure 5B**, "Step 4"). Finally, the movie of these projected images was further stabilized in
952 three successive steps: (i.) matching each frame to the average of the first 50 frames, (ii.)
953 matching each frame of the resulting movie iteratively to its neighbor, (iii.) matching each frame
954 of the resulting movie to the average of the first 50 frames (**Figure 5B**, "Step 5").

955 To estimate the degree of brain motion of ChP *in vivo,* we quantified the two kinds of
956 correction for brain motion that were applied (see above). The first correction involved intra-
957 volume XY displacements for each plane (**Figure 5B,** "Step 2"). The second involved inter-
958 volume displacements from 3D translational registration (**Figure 5B,** "Step 3"), together with
959 additional XY displacements common to all planes and derived from the registration of the 2D
960 image stack resulting from axial mean projections of each volume (**Figure 5B,** "Step 5"). The
961 intra-volume XY displacement reflected faster frame-to-frame motion within a given Z-scan
962 (12.8-31 frames per second; 31-81 frames per volume). We quantified the distribution of intra-

963 volume XY displacements using the Euclidean distance of intra-volume shifts in X and Y. We
964 also calculated inter-volume displacements between successive volumes (0.16-0.97 volumes per
965 second) to estimate the level of motion observed at these somewhat slower timescales (using the
966 using the Euclidean distance of X and Y displacements between consecutive volumes, ΔXY, and
967 using the absolute value of the shift in Z between consecutive volumes). These distributions were
968 then expressed as cumulative distribution functions for each recording (**Figures 5G and 5H**).
969 Overall, the degree of brain motion was substantially larger than what is observed for recordings
970 in other brain regions such as in the neocortex.
971
972 **Inter-volume motion artifacts**
973 To assess the efficacy of our 3D registration in removing motion artifacts, we considered sets of
974 five consecutive volumes of the red channel (vasculature), which was expected to be stable (i.e.
975 near-constant voxel intensity) in the absence of brain motion at this timescale. Thus, we used the
976 metric of local standard deviation as a proxy for inter-volume motion artifacts. A rolling standard
977 deviation across five neighboring volumes was calculated for each 3D voxel. These standard
978 deviation contributions were averaged to obtain a global estimate of image stability. To account
979 for global intensity changes within and across recordings, we normalized this mean standard
980 deviation signal by the mean fluorescence to obtain an estimate of inter-volume motion artifacts
981 over time.
982
983 **Re-registration of single-cell regions**
984 After 3D registration of the entire region, individual cell regions of interest (ROIs) were selected
985 for local re-registration. XYZ regions were determined manually. The selected regions were then

986 re-registered in XY with Fourier transformation-based cross-correlation, and individual plane
987 affine registration, as described in the "3D registration" section, above.
988
989 **Recording "physiological housekeeping" by immune cells**
990 To assess the uptake of dextran by immune cells, a 3D recording of the ChP was acquired for 1
991 hour before the injection of 70 kDa red dextran. Immediately after this recording, without
992 moving the recording field of view, the mouse was injected with 70 kDa red dextran, and
993 recorded for 1 hour, as the dextran filled the vessels. Another 48 hours later, using local vascular
994 features and tissue morphology, we imaged the same volume of ChP for an additional hour,
995 without injecting more red dextran. All three recordings used the same acquisition parameters.
996
997 **LPS RESPONSE**
998 To elicit a peripheral inflammatory response, 0.5 mg/kg lipopolysaccharide (LPS, Sigma) was
999 delivered IP (Monje et al., 2003). An equal volume of saline was used as a control.
1000
1001 **Quantifying *in vitro* "vessel coating" by immune cells**
1002 To quantify immune cell alignment with the periluminal region immediately adjacent to
1003 vessels, wholemount LV ChP explants of LPS- and saline-injected $Cx_3cr_1^{+/GFP}$ mice were
1004 isolated and immunostained for GFP to label immune cells, and PECAM to label vasculature.
1005 Using a 500 pixel x 500 pixel ROI (225 x 225 μm^2), the image pixel intensities were rescaled to
1006 the range 0-1 (20^{th} percentile of pixel brightness rescaled to 0; 90^{th} percentile of pixel brightness
1007 rescaled to 1). A first step to defining the periluminal region was to develop an automated
1008 algorithm to segment the vasculature. Segmenting vasculature involved identifying image

regions that contain tube-like structures. Additionally, these tubes may be of different sizes (e.g., capillaries vs. veins), and may also join together in junctions. Based on this structural description, a Jerman filter (Jerman et al., 2016) based on the local second-order derivative of the image (filter widths from 8 to 15 pixels; regularization factor $\tau = 1$) was used to enhance pixels that were part of tube-like structures. The resulting image was then binarized to separate vasculature from the background.

To validate the automated vessel segmentation algorithm used as an initial step towards defining periluminal space surrounding vessels, the vasculature image was manually segmented as a ground truth comparison. Using the Selection Brush tool in Fiji, the vessels were hand traced and converted to a manual binary mask. The same region was automatically segmented, as above, to generate an automatic binary mask. The automated and binary masks were compared with the contour matching function, bfscore.m, in MATLAB. Briefly, the Boundary F1 score measures the how closely a predicted boundary matches a ground truth boundary. This algorithm was chosen over Dice or Jaccard similarity coefficients, as our principal goal involved defining the accuracy of the estimate of periluminal boundary.

To obtain an estimate of periluminal space, the edge of the binary image of vasculature (see above) was then dilated with a disk kernel with a width of 5 pixels (~1.6 μm). Pixels belonging to this dilated mask but not to the original vascular mask were considered to belong to the periluminal region.

Pixels containing immune cell bodies or processes were defined as follows, from the green emission image. First, the image pixel intensities were rescaled to the range 0-1 (10^{th} percentile of pixel brightness rescaled to 0; 98^{th} percentile of pixel brightness rescaled to 1). The image was then binarized, and dilated using a disk kernel with a width of 5 pixels. The degree of

immune cell process occupancy within the periluminal region ("vessel coating") was estimated as the proportion of vessel edge that overlapped with the binarized and dilated immune cells.

***In vivo* vessel coating**

To quantify *in vivo* changes in immune cell occupancy of periluminal regions near vessels in response to LPS, a four-hour, four-dimensional (X Y x Z x T stack) dataset was mean-projected along the Z-axis to produce an XYT image stack. This image stack was downsampled to 120 volumes (by averaging successive sets of 30 volumes), to improve the signal-to-noise ratio. This image stack was split into two channels: immune cells and vasculature. To define the periluminal region, vascular image stack intensity levels were rescaled to the range 0-1 (20^{th} percentile of pixel brightness rescaled to 0; 98^{th} percentile of pixel brightness rescaled to 1), and registered using the MultiStackReg function in Fiji, based on motion estimates from the immune cell image stack (NIH). A median projection of the vascular channel was computed, and pixels belonging to vessels were enhanced relative to the background using a Jerman filter (Jerman et al., 2016)(filter width from 8 to 10 pixels; regularization factor, $\tau = 1$; see above). The gradient of the Jerman filtered image was calculated to find the vessel edges, and the gradient image was binarized, and morphologically closed (dilation, followed by erosion of a binary image, resulting in the filling of small holes; the structuring element was a disk with radius of 2 pixels), defining the periluminal regions of the image.

The immune cell image stack intensity levels were rescaled to the range 0-1 (10^{th} percentile of pixel brightness levels, rescaled to 0; 98^{th} percentile of pixel brightness levels, rescaled to 1). For each time frame in the image stack, t, the fluorescence in the periluminal region, F(t) was calculated as mean pixel intensity in the periluminal region defined above.

GFP fluorescence in the periluminal region, F(t), was measured at each frame in the image stack as the mean immune cell pixel intensity in the periluminal region defined above. The average fluorescence in the 1 hour prior to LPS injection was used as a baseline, F_0. Change in fluorescence in response to LPS was expressed as: $\Delta F/F_0$.

IMMUNE CELL IMAGING DURING ACUTE ChP INJURY

In this experiment, a local region of the ChP of an adult awake mouse was heated using the imaging laser, together with two-photon imaging of immune cells and vasculature prior to and following the heating. After one hour of imaging of 3D volumes of immune cells and vasculature (as detailed above) at 2x magnification and 30-40 mW power, the scan settings were changed to 8x magnification and ~150 mW for two minutes to induce focal heating of a local region of the tissue. Immediately following this tissue manipulation, the previous laser scanning settings were returned to observe immune cell activity in response to the focal damage.

Tracking immune cell acute response to laser burn injury

Immune cell body positions relative to the rectangular region targeted for focal laser heating were sampled every 5 minutes for 30 minutes before heating and in the one hour after heating. A distance transformation was used to calculate the closest distance from each cell to the rectangular injury site at each timepoint (using bwdist.m in MATLAB). Velocities of these cells toward the burn site ($\Delta\, distance/\Delta\, time$) were calculated for the 30-minute period before the injury, and separately for the 60-minute period after the injury. In cases where the cell entered the burn site prior to the end of the recording period, the velocity was calculated using the displacement that took place until the moment that the cell entered the burn site.

OTHER SUPPORTING EXPERIMENTS

Immunostaining and immunoblotting

ChP explants were dissected and fixed in 4% paraformaldehyde for 10 min at room temperature. Samples were incubated in primary antibodies overnight at 4°C and in secondary antibodies at room temperature for two hours. For ACTA2 staining, samples were permeabilized with 0.1% Tween 20 in PBS prior to primary antibody incubation. For GFP and CD31 staining, samples were blocked (0.3% TritonX-100, 5% goat serum in PBS) for 1 hour prior to primary antibody incubation. All samples were counterstained with Hoechst 33342 (Invitrogen, H3570, 1:10,000) and mounted onto slides using Fluoromount-G (SouthernBiotech). Standard protocols were used for immunoblotting.

Nearest-neighbor analysis

Locations of cell centers were selected using the Cell Counter plugin in Fiji. The tissue outline was drawn manually and made into a binary mask using Fiji. The nearest-neighbor distance was calculated for each individual cell, and the cumulative distribution function was plotted using the spatstat package in R (Baddedy et al., 2015).

Simulated distributions based on a 2D Poisson distribution were generated iteratively 100 times. The mean of these simulated distributions yielded the “Poisson” estimate, while their extrema yielded a $p = 0.01$ acceptance interval.

Cytokine FACS array

Pure CSF samples were collected from the cisterna magna. Blood samples were collected by tail-nick one hour following saline or LPS injection. The samples were coagulated, centrifuged and diluted five-fold. Post-surgical CSF samples were diluted two- or three-fold; post-LPS CSF samples were not diluted. For the 13-plex cytokine FACS-ELISA analysis, all samples were processed according to the manufacturer's instructions. After resuspension, the beads were run on a FACS Celesta (BD Biosciences) and FACS results were analyzed by LegendPlex v7.1 software.

Quantitative RT-PCR

RNA samples were prepared using either the RecoverAll Total Nucleic Acid Isolation Kit (Ambion) or the mirVana miRNA isolation kit, following the manufacturer's specifications. Extracted RNA was quantified spectrophotometrically and 100 ng was reverse-transcribed into cDNA using the ImProm-II Reverse Transcription System (Promega) or ABI High Capacity cDNA Reverse Transcription Kit (4368813, Thermo Fisher). Primers were purchased from Thermo Fisher (Taqman Gene expression assays, informed by "Best Coverage") and q-PCR reactions were conducted performed in duplicate using Taqman Fast Univ. PCR Master Mix. Cycling was executed using the StepOnePlus Real-Time PCR System (Invitrogen) and analysis of relative gene expression was performed using the $2^{-\Delta\Delta CT}$ method (Livak and Schmittgen, 2001). Gene expression readouts were normalized to eukaryotic *18S* rRNA or *Gapdh* as internal controls.

Transmission and Scanning EM

Lateral ventricle ChP tissue from adult mouse brain was micro-dissected and processed for EM using standard methods (Coulter et al., 2018).

QUANTIFICATION AND STATISTICAL ANALYSIS

To achieve robust and unbiased results while minimizing animal use, whenever possible, we focused on within-mouse comparisons (e.g. changes in immune cell motility before and after tissue injury, **Figure 7I**), which affords greater sensitivity. It was not possible for experimenter to be not blinded to experimental conditions, except in analysis of LPS vs. saline control (**Figure 7C**). We attempted to adhere to principles of Good Laboratory Practice (www.who.int/tdr/publications/documents/glp-handbook.pdf). Unbiased results were obtained by prospectively defining exclusion criteria (e.g., acquisition criteria [alignment, image quality], viral expression/localization). All descriptions of statistical significance, statistical tests used, and exact values and representations of n can be found in the figure legends. Software packages used for statistical tests can be found in the STAR methods Key Resource Table under Software and Algorithms.

SUPPLEMENTAL VIDEO LEGENDS

Video S1. Imaging calcium activity in adult lateral ventricle ChP explant. Related to Figure 1. Widefield epifluorescence imaging of spontaneous calcium activity of epithelial cells in ChP explants (large leaf of LV ChP) in *FoxJ1-Cre::Ai95D* mice. This method allowed for simultaneous visualization of activity in many thousands of active epithelial cells (see also **Figure 1F**). *Inset*: zoom-in of cellular activity in the region outlined by a solid white square

(same subregion as in **Figures 1G-1M**, spanning 161 x 161 μm^2). Note uncorrelated activity throughout the explant. Timestamps are in units of minutes:seconds.

Video S2. **Epithelial cells show spontaneous and evoked calcium activity in explants. Related to Figure 2.** Widefield epifluorescence imaging of spontaneous calcium activity of epithelial cells in ChP explants (large leaf of LV ChP) in *FoxJ1-Cre::Ai95D* mice during delivery of 5 nM, 50 nM and 500 nM doses of 5-HT, indicated at top of movie. *Left:* raw movie. *Right:* change in fluorescence from pre-drug baseline. Note the increasing magnitude of responses to progressively larger doses of 5-HT. Note also the progressive decline in spontaneous activity following drug administration. Movie data and dimensions are same as in **Figure 2A**. Timestamps are in units of minutes:seconds.

Video S3. Epithelial cells show spontaneous and evoked calcium activity that can stimulate exocrine secretory events in explants. Related to Figure 2. Two-photon calcium imaging of a LV ChP explant from a *FoxJ1-Cre::Ai95D* mouse during delivery of 5 nM, 50 nM, and 500 nM doses of the 5-HT_{2C}-specific agonist, WAY-161503. Movie data and dimensions are same as in **Figure 2F**. Timestamps are in units of minutes:seconds. The larger the dose, the more cells showed sustained evoked increases in calcium, followed by apocrine secretion events involving gradual pinching off and release of intracellular contents (see, for example, minutes 32-44 of the video).

Video S4. Cultured ChP cell shows spontaneous vesicle fusion events. Related to Figure 2. TIRF imaging of VAMP3-pHluorin from Z310 cultured ChP cell shows spontaneous vesicle fusion events (brief, bright dots). Movie data and dimensions are same as in **Figure S2K**. Scale in first frame, 10 μm. Timestamps are in units of minutes:seconds.

Video S5. Epithelial cell shows spontaneous and evoked vesicle fusion events in explants. Related to Figure 2. Confocal imaging of a single cultured LV ChP epithelial cell exhibiting increased frequency of VAMP3-related vesicle release events following delivery of the 5-HT_{2C} agonist WAY-161503 (500 nM). *Left:* raw confocal images. *Right*: spatially filtered images (see **Figure 2G** and associated legend for details). Movie data and dimensions are same as in **Figure 2G**. Scale in first frame, 5 μm. Timestamps are in units of minutes:seconds.

Video S6. Imaging lateral ventricle ChP in awake mice. Related to Figure 3. Epifluorescence imaging from four awake mice (*FoxJ1-Cre::Ai95D*) with surgically implanted imaging cannulae and windows highlighting typical motion of LV ChP (bright tissue in center) over a 30-second period. These four mice were imaged at 134, 123, 325, and 349 days post-surgery, respectively. Timestamps are in units of minutes:seconds. Note that mice shown here are different than those in **Figure 3F**.

Video S7. Spontaneous *in vivo* calcium activity of epithelial cells reveals subcellular activity. Related to Figure 4. Two-photon imaging of spontaneous subcellular calcium activity of ChP epithelial cells in an awake mouse (*FoxJ1-Cre::Ai95D*) over 16 seconds. The movie was filtered

using a 2D spatial Gaussian (sigma: 0.55 μm), and a 1-dimensional Gaussian in time (sigma: 0.033 s). Dimensions of the movie are: 282 x 282 μm^2. Timestamps are in units of minutes:seconds.

Video S8. Spontaneous *in vivo* calcium activity of epithelial cells shows subcellular activity in a second mouse. Related to Figure 4. Two-photon imaging of spontaneous subcellular calcium activity of ChP epithelial cells in an awake mouse (*FoxJ1-Cre::Ai95D*) over 6 seconds (similar to **Video S7**, but from a second mouse). Timestamps are in units of minutes:seconds. Movie data and dimensions are same as in **Figure 4D**.

Video S9. Epithelial cells show spontaneous and evoked calcium activity that can stimulate exocrine secretory events *in vivo*. Related to Figure 4. *In vivo* two-photon calcium imaging of LV ChP epithelial cells (*FoxJ1-Cre::Ai95D* mouse) prior to and following delivery of a 5-HT_{2C}-specific agonist, WAY-161503 (3 mg/kg, SC). Movie data and dimensions are same as in **Figure 4L**. Timestamps in top left corner indicate times after injection of WAY-161503, in units of hours:minutes:seconds. Note the elevation in calcium in each cell, followed by apocrine secretion events involving release of intracellular contents including GCaMP6f protein into the CSF.

Video S10. Individual epithelial cells show spontaneous and evoked calcium activity that can stimulate exocrine secretory events *in vivo*. Related to Figure 4. Zoom-in from an *in vivo* two-photon imaging session involving three individual epithelial cells expressing GCaMP6f

(from a *FoxJ1-Cre::Ai95D* mouse) following injection of a 5-HT_{2C}-specific agonist, WAY-161503 (3 mg/kg SC; see also **Video S9**). Note the apocrine secretion events involving release of intracellular contents including GCaMP6f into the CSF. Timestamps are in units of minutes:seconds. Movie data and dimensions for cell in left panel are same as in **Figure 4M**; other panels show two additional example cells (same dimensions).

Video S11. *In vivo* imaging of *$Cx_3cr_1^{+/GFP}$* ChP immune cells reveals diverse functions including local surveillance. Related to Figure 5. Four hour imaging dataset (maximum intensity projections of two-photon imaging volumes, similar to **Figure 5A**) demonstrates immune cells (green, *$Cx_3cr_1^{+/GFP}$* mouse) surveying LV ChP vasculature (red, labeled using subcutaneous injection of Texas Red dextran). Scale in first frame: 50 μm. Timestamps are in units of hours:minutes:seconds.

Video S12. Illustration of within-volume brain motion. Related to Figure 5. Pan through of a single imaging volume (duration of acquisition of each volume was 6.33 s, and each volume consisted of 81 planes spanning 400 μm in depth), from a volumetric imaging run collected in an awake head-fixed mouse running on a trackback (*top left*). We used multi-color two-photon imaging of Texas Red-labeled vessels and *$Cx_3cr_1^{+/GFP}$* immune cells, with Z-scanning enabled by a piezoelectric objective stage. Note the X-Y shifts across planes of this volume. We thus sequentially aligned each frame to a common reference using a translational alignment procedure (see also **Figures 5B-5D**). The degree that we shifted each frame in X and in Y directions is illustrated at bottom. The resulting aligned volume is shown at top right (blue regions indicate

areas where no data is available due to alignment shifts in the imaging plane). Each frame spans 255 x 255 μm^2.

Video S13. Additional movies from *in vivo* imaging of individual *Cx$_3$cr$_1^{+/GFP}$* ChP immune cells indicates multiple cell subtypes. Related to Figure 6. Individual *Cx$_3$cr$_1^{+/GFP}$* immune cells surveying the LV ChP across a 44-minute period. Timestamps are in units of minutes:seconds. Dimensions for movies in top left, top right, bottom left, and bottom right panels are same as in **Figures 6D**-**6G**, respectively. *Top left*: epiplexus immune cell that moves freely over neighboring vessels because it is on the apical surface of the ChP. *Top right*: stromal immune cell with cell body that remains in place, but with processes extending beyond neighboring vasculature and then retracting due to apparent contact mediated inhibition with a neighboring process. *Bottom left*: stromal immune cell whose processes travel along vasculature, exhibiting contact mediated inhibition after touching processes from neighboring cells, and contact with one of its own processes. *Bottom right*: stromal immune cell with mobile cell body whose mobility appears constrained by the surrounding vessels, but whose processes extend beyond these vessels.

Video S14. Uptake of dextran by stromal ChP immune cells. Related to Figure 6. Individual *Cx$_3$cr$_1^{+/GFP}$* immune cells surveying the LV ChP across a 61-minute period following IP injection of Texas Red dextran (70 kDa) in awake mice. Note the gradual uptake of dextran in immune cell processes in the periluminal region near vessels (**Figure 6I**). Scale, 25 μm. Timestamps are in units of hours:minutes:seconds.

Video S15. Identification of stromal and epiplexus cells in the ChP during dextran uptake. Related to Figure 6. 48 hours after IP injection of Texas Red dextran (70 kDa) (**Figure 6H**), some immune cells accumulated dextran in their processes and cell bodies while others did not. Here, we characterize the immune cells that did not uptake dextran by labeling with white circles in a scan through the tissue. We then considered a maximum intensity projection image from the same volume (middle of video), and inspected X-Z and Y-Z cross-section scans of the volume (rectangular movies at end of video; location of each cross section indicated by yellow and cyan lines through the maximum intensity image). Note that most immune cells that did not uptake dextran were located out of the central, vascular layer of the ChP and were classified as epiplexus cells. Scale, 50 μm.

Video S16. ChP immune cells respond to systemic injury. Related to Figure 7. *In vivo* two-photon imaging of LV ChP immune cells (*Cx3cr1*$^{+/GFP}$ mouse) during IP delivery of LPS (5 mg/kg). Immune cells flatten in the periluminal region near vessels (red) in response to LPS at ~1 hour post-LPS (indicated at top of movie). Timestamps are in units of hours:minutes (13 minutes/frame). Movie data are same as in **Figure 7D**. Dimensions of the movie are: 97 x 90 μm^2. Note that many but not all immune cells respond to LPS. White arrowhead tracks an immune cell that flattens into the periluminal region.

Video S17. ChP immune cells respond to acute injury. Related to Figure 7. *In vivo* two-photon imaging of LV ChP immune cells (*Cx3cr1*$^{+/GFP}$ mouse) during focal laser heating within

the region outlined by a white square. Approximately 6 minutes post-burn, Texas Red dextran leaks out from damaged vessels. Some nearby immune cells change to an activated state with retracted processes and migrate to the site of injury immediately following focal laser heating. After reaching the site of injury, these cells aggregate and remain stationary. Other immune cells appear unaffected. Movie data are same as in **Figure 7H**. Timestamps indicate time since focal laser heating and are in units of hours:minutes:seconds. Scale, 50 μm. See also **Video S18**.

Video S18. Identification of stromal and epiplexus immune cells in the ChP during a focal injury model. Related to Figure 7. Following a focal ChP injury induced by laser heating (**Figures 7G and 7H**), some immune cell bodies moved towards the injury site while others did not. Here, we characterized the immune cells that did move towards the injury by labeling them with white circles in a flythrough of the imaging volume (beginning of video; snapshot at 25 minutes following laser burn). We then considered a maximum intensity projection image from the same volume (middle of video), and inspected various X-Z and Y-Z cross-sections of the volume (rectangular movies at end of video; location of each cross-section indicated by yellow and cyan lines through the maximum intensity projection image). Note that most immune cells that later moved towards the site of injury (6/8 mobile cells) were located outside of the central, vascular layer of the ChP, and were thereby characterized as epiplexus cells. Scale, 50 μm.

REFERENCES

Agnew, W.F., Yuen, T.G., and Achtyl, T.R. (1980). Ultrastructural observations suggesting apocrine secretion in the choroid plexus: a comparative study. Neurol Res *1*, 313–332.

Ambudkar, I. (2018). Calcium signaling defects underlying salivary gland dysfunction. Biochim. Biophys. Acta - Mol. Cell Res. *1865*, 1771–1777.

Ambudkar, I.S. (2016). Calcium signalling in salivary gland physiology and dysfunction. J. Physiol. *594*, 2813–2824.

Audhya, T., Adams, J.B., and Johansen, L. (2012). Correlation of serotonin levels in CSF, platelets, plasma, and urine. Biochim. Biophys. Acta - Gen. Subj. *1820*, 1496–1501.

Baddedy, A., Rubak, E., and Turner, R. (2015). Spatial Point Patterns: Methodology and Applications with R (Chapman and Hall/CRC Press).

Balaji, R., Bielmeier, C., Harz, H., Bates, J., Stadler, C., Hildebrand, A., and Classen, A.-K. (2017). Calcium spikes, waves and oscillations in a large, patterned epithelial tissue. Sci. Rep. *7*, 42786.

Balusu, S., Brkic, M., Libert, C., and Vandenbroucke, R.E. (2016a). The choroid plexus-cerebrospinal fluid interface in Alzheimer's disease: more than just a barrier. Neural Regen Res *11*, 534–537.

Balusu, S., Van Wonterghem, E., De Rycke, R., Raemdonck, K., Stremersch, S., Gevaert, K., Brkic, M., Demeestere, D., Vanhooren, V., Hendrix, A., et al. (2016b). Identification of a novel mechanism of blood–brain communication during peripheral inflammation via choroid plexus-derived extracellular vesicles. EMBO Mol. Med. *8*, 1162–1183.

Cloutier, N., Pare, A., Farndale, R.W., Schumacher, H.R., Nigrovic, P.A., Lacroix, S., and Boilard, E. (2012). Platelets can enhance vascular permeability. Blood *120*, 1334–1343.

Cocucci, E., Aguet, F., Boulant, S., and Kirchhausen, T. (2012). The first five seconds in the life of a clathrin-coated pit. Cell *150*, 495–507.

Concepcion, A.R., and Feske, S. (2017). Regulation of epithelial ion transport in exocrine glands by store-operated Ca2+ entry. Cell Calcium *63*, 53–59.

Conn, P.J., and Sanders-Bush, E. (1986). Agonist-induced phosphoinositide hydrolysis in choroid plexus. J Neurochem *47*, 1754–1760.

Coulter, M.E., Dorobantu, C.M., Lodewijk, G.A., Delalande, F., Cianferani, S., Ganesh, V.S., Smith, R.S., Lim, E.T., Xu, C.S., Pang, S., et al. (2018). The ESCRT-III Protein CHMP1A Mediates Secretion of Sonic Hedgehog on a Distinctive Subtype of Extracellular Vesicles. Cell Rep *24*, 973-986 e8.

Crossgrove, J.S., Li, G.J., and Zheng, W. (2005). The choroid plexus removes beta-amyloid from brain cerebrospinal fluid. Exp. Biol. Med. (Maywood). *230*, 771–776.

Damkier, H.H., Brown, P.D., and Praetorius, J. (2013). Cerebrospinal Fluid Secretion by the Choroid Plexus. Physiol. Rev. *93*, 1847–1892.

Dani, N., Herbst, R.H., Habib, N., Head, J., Dionne, D., Nguyen, L., McCabe, C., Cui, J., Shipley, F.B., Jang, A., et al. (2019). A cellular and spatial map of the choroid plexus across brain ventricles and ages. BioRxiv 627539.

Davalos, D., Grutzendler, J., Yang, G., Kim, J. V, Zuo, Y., Jung, S., Littman, D.R., Dustin, M.L., and Gan, W.-B. (2005). ATP mediates rapid microglial response to local brain injury in vivo. Nat. Neurosci. *8*, 752–758.

Doench, J.G., Fusi, N., Sullender, M., Hegde, M., Vaimberg, E.W., Donovan, K.F., Smith, I., Tothova, Z., Wilen, C., Orchard, R., et al. (2016). Optimized sgRNA design to maximize activity and minimize off-target effects of CRISPR-Cas9. Nat. Biotechnol. *34*, 184–191.

Dombeck, D.A., Khabbaz, A.N., Collman, F., Adelman, T.L., and Tank, D.W. (2007). Imaging Large-Scale Neural Activity with Cellular Resolution in Awake, Mobile Mice. Neuron *56*, 43–57.

Dombeck, D.A., Harvey, C.D., Tian, L., Looger, L.L., and Tank, D.W. (2010). Functional imaging of hippocampal place cells at cellular resolution during virtual navigation. Nat Neurosci *13*, 1433–1440.

Esterle, T.M., and Sanders-Bush, E. (1992). Serotonin agonists increase transferrin levels via activation of 5-HT1C receptors in choroid plexus epithelium. J. Neurosci. *12*, 4775–4782.

Fame, R.M., and Lehtinen, M.K. (2020). Emergence and Developmental Roles of the Cerebrospinal Fluid System. Dev. Cell *52*, 261–275.

Farkaš, R. (2015). Apocrine secretion: New insights into an old phenomenon.

Ghersi-Egea, J.-F., Strazielle, N., Catala, M., Silva-Vargas, V., Doetsch, F., and Engelhardt, B. (2018). Molecular anatomy and functions of the choroidal blood-cerebrospinal fluid barrier in health and disease. Acta Neuropathol. *135*, 337–361.

Goldey, G.J., Roumis, D.K., Glickfeld, L.L., Kerlin, A.M., Reid, R.C., Bonin, V., Schafer, D.P., and Andermann, M.L. (2014). Removable cranial windows for long-term imaging in awake mice. Nat Protoc *9*, 2515–2538.

Gonzalez, A., Leadbeater, W.E., Burg, M., Sims, K., Terasaki, T., Johanson, C.E., Stopa, E.G., Eliceiri, B.P., and Baird, A. (2011). Targeting choroid plexus epithelia and ventricular ependyma for drug delivery to the central nervous system. BMC Neurosci. *12*, 4.

Gudeman, D.M., Nelson, S.R., and Merisko, E.M. (1987). Protein secretion by choroid plexus: Isolated apical fragments synthesize protein in vitro. Tissue Cell *19*, 101–109.

Gudeman, D.M., Brightman, M.W., Merisko, E.M., and Merril, C.R. (1989). Release from live choroid plexus of apical fragments and electrophoretic characterization of their synthetic products. J Neurosci Res *24*, 184–191.

Guizar-Sicairos, M., and Fienup, J.R. (2008). Direct image reconstruction from a Fourier intensity pattern using HERALDO. Opt. Lett. *33*, 2668.

Haddad, M.R., Donsante, A., Zerfas, P., and Kaler, S.G. (2013). Fetal Brain-directed AAV Gene Therapy Results in Rapid, Robust, and Persistent Transduction of Mouse Choroid Plexus Epithelia. Mol. Ther. - Nucleic Acids *2*, e101.

Hickman, S., Izzy, S., Sen, P., Morsett, L., and El Khoury, J. (2018). Microglia in neurodegeneration. Nat Neurosci *21*, 1359–1369.

Hierro-Bujalance, C., Bacskai, B.J., and Garcia-Alloza, M. (2018). In Vivo imaging of microglia with multiphoton microscopy. Front. Aging Neurosci. *10*, 218.

Van Hove, H., Martens, L., Scheyltjens, I., De Vlaminck, K., Pombo Antunes, A.R., De Prijck, S., Vandamme, N., De Schepper, S., Van Isterdael, G., Scott, C.L., et al. (2019). A single-cell atlas of mouse brain macrophages reveals unique transcriptional identities shaped by ontogeny and tissue environment. Nat. Neurosci. *22*, 1021–1035.

Hudry, E., and Vandenberghe, L.H. (2019). Therapeutic AAV Gene Transfer to the Nervous System: A Clinical Reality. Neuron *101*, 839–862.

Hudson, A.J. (1960). The development of the vascular pattern of the choroid plexus of the lateral

ventricles. J Comp Neurol *115*, 171–186.

Jerman, T., Pernus, F., Likar, B., and Spiclin, Z. (2016). Enhancement of Vascular Structures in 3D and 2D Angiographic Images. IEEE Trans. Med. Imaging *35*, 2107–2118.

Jung, S., Aliberti, J., Graemmel, P., Sunshine, M.J., Kreutzberg, G.W., Sher, A., and Littman, D.R. (2000). Analysis of Fractalkine Receptor CX3CR1 Function by Targeted Deletion and Green Fluorescent Protein Reporter Gene Insertion. Mol. Cell. Biol. *20*, 4106–4114.

Karimy, J.K., Zhang, J., Kurland, D.B., Theriault, B.C., Duran, D., Stokum, J.A., Furey, C.G., Zhou, X., Mansuri, M.S., Montejo, J., et al. (2017). Inflammation-dependent cerebrospinal fluid hypersecretion by the choroid plexus epithelium in posthemorrhagic hydrocephalus. Nat. Med. *23*, 997–1003.

Kierdorf, K., Masuda, T., Jordão, M.J.C., and Prinz, M. (2019). Macrophages at CNS interfaces: ontogeny and function in health and disease. Nat. Rev. Neurosci. *20*, 547–562.

Kim, S., Hwang, Y., Lee, D., and Webster, M.J. (2016). Transcriptome sequencing of the choroid plexus in schizophrenia. Transl Psychiatry *6*, e964.

Lehtinen, M.K., Zappaterra, M.W., Chen, X., Yang, Y.J., Hill, A.D., Lun, M., Maynard, T., Gonzalez, D., Kim, S., Ye, P., et al. (2011). The Cerebrospinal Fluid Provides a Proliferative Niche for Neural Progenitor Cells. Neuron *69*, 893–905.

Lein, E.S., Hawrylycz, M.J., Ao, N., Ayres, M., Bensinger, A., Bernard, A., Boe, A.F., Boguski, M.S., Brockway, K.S., Byrnes, E.J., et al. (2007). Genome-wide atlas of gene expression in the adult mouse brain. Nature *445*, 168–176.

Li, Q., and Barres, B.A. (2018). Microglia and macrophages in brain homeostasis and disease. Nat. Rev. Immunol. *18*, 225–242.

Liang, L., Fratzl, A., Goldey, G., Ramesh, R.N., Sugden, A.U., Morgan, J.L., Chen, C., and Andermann, M.L. (2018). A Fine-Scale Functional Logic to Convergence from Retina to Thalamus. Cell *173*, 1343-1355 e24.

Livak, K.J., and Schmittgen, T.D. (2001). Analysis of relative gene expression data using real-time quantitative PCR and the 2-ΔΔCT method. Methods *25*, 402–408.

Lun, M.P., Johnson, M.B., Broadbelt, K.G., Watanabe, M., Kang, Y. -j., Chau, K.F., Springel, M.W., Malesz, A., Sousa, A.M.M., Pletikos, M., et al. (2015a). Spatially Heterogeneous Choroid Plexus Transcriptomes Encode Positional Identity and Contribute to Regional CSF Production. J. Neurosci. *35*, 4903–4916.

Lun, M.P., Monuki, E.S., and Lehtinen, M.K. (2015b). Development and functions of the choroid plexus-cerebrospinal fluid system. Nat. Rev. Neurosci. *16*, 445–457.

Madisen, L., Garner, A.R., Shimaoka, D., Chuong, A.S., Klapoetke, N.C., Li, L., van der Bourg, A., Niino, Y., Egolf, L., Monetti, C., et al. (2015). Transgenic Mice for Intersectional Targeting of Neural Sensors and Effectors with High Specificity and Performance. Neuron *85*, 942–958.

Marques, F., Sousa, J.C., Coppola, G., Falcao, A.M., Rodrigues, A.J., Geschwind, D.H., Sousa, N., Correia-Neves, M., and Palha, J.A. (2009). Kinetic profile of the transcriptome changes induced in the choroid plexus by peripheral inflammation. J. Cereb. Blood Flow Metab. *29*, 921–932.

Marques, F., Sousa, J.C., Sousa, N., and Palha, J.A. (2013). Blood-brain-barriers in aging and in

Alzheimer's disease. Mol Neurodegener *8*, 38.

Mesa, K.R., Rompolas, P., Zito, G., Myung, P., Sun, T.Y., Brown, S., Gonzalez, D.G., Blagoev, K.B., Haberman, A.M., and Greco, V. (2015). Niche-induced cell death and epithelial phagocytosis regulate hair follicle stem cell pool. Nature *522*, 94–97.

Monje, M.L., Toda, H., and Palmer, T.D. (2003). Inflammatory Blockade Restores Adult Hippocampal Neurogenesis. Science (80-.). *302*, 1760 LP – 1765.

Mottahedin, A., Joakim Ek, C., Truvé, K., Hagberg, H., and Mallard, C. (2019). Choroid plexus transcriptome and ultrastructure analysis reveals a TLR2-specific chemotaxis signature and cytoskeleton remodeling in leukocyte trafficking. Brain. Behav. Immun. *79*, 216–227.

Mukamel, E., Nimmerjahn, A., and Schnitzer, M. (2009). Automated analysis of cellular signals from large-scale calcium imaging data. Neuron *63*, 747–760.

Narboux-Neme, N., Pavone, L.M., Avallone, L., Zhuang, X., and Gaspar, P. (2008). Serotonin transporter transgenic (SERTcre) mouse line reveals developmental targets of serotonin specific reuptake inhibitors (SSRIs). Neuropharmacology *55*, 994–1005.

Narciso, C.E., Contento, N.M., Storey, T.J., Hoelzle, D.J., and Zartman, J.J. (2017). Release of Applied Mechanical Loading Stimulates Intercellular Calcium Waves in Drosophila Wing Discs. Biophys. J. *113*, 491–501.

Netsky, M., and Shuangshoti, S. (1975). The choroid plexus in health and disease.

Okaty, B.W., Sturrock, N., Escobedo Lozoya, Y., Chang, Y.J., Senft, R.A., Lyon, K.A., Alekseyenko, O. V., and Dymecki, S.M. (2020). A single-cell transcriptomic and anatomic atlas of mouse dorsal raphe Pet1 neurons. Elife *9*.

Pellegrini, L., Bonfio, C., Chadwick, J., Begum, F., Skehel, M., and Lancaster, M.A. (2020). Human CNS barrier-forming organoids with cerebrospinal fluid production. Science (80-.). *369*, eaaz5626.

Pozner, A., Xu, B., Palumbos, S., Gee, J.M., Tvrdik, P., and Capecchi, M.R. (2015). Intracellular calcium dynamics in cortical microglia responding to focal laser injury in the PC::G5-tdT reporter mouse. Front. Mol. Neurosci. *8*, 12.

Reboldi, A., Coisne, C., Baumjohann, D., Benvenuto, F., Bottinelli, D., Lira, S., Uccelli, A., Lanzavecchia, A., Engelhardt, B., and Sallusto, F. (2009). C-C chemokine receptor 6–regulated entry of TH-17 cells into the CNS through the choroid plexus is required for the initiation of EAE. Nat. Immunol. *10*, 514–523.

Rompolas, P., Mesa, K.R., Kawaguchi, K., Park, S., Gonzalez, D., Brown, S., Boucher, J., Klein, A.M., and Greco, V. (2016). Spatiotemporal coordination of stem cell commitment during epidermal homeostasis. Science (80-.). *352*, 1471–1474.

Rosenzweig-Lipson, S., Zhang, J., Mazandarani, H., Harrison, B.L., Sabb, A., Sabalski, J., Stack, G., Welmaker, G., Barrett, J.E., and Dunlop, J. (2006). Antiobesity-like effects of the 5-HT2C receptor agonist WAY-161503. Brain Res *1073–1074*, 240–251.

Samanta, K., and Parekh, A.B. (2016). Store-operated Ca2+ channels in airway epithelial cell function and implications for asthma. Philos. Trans. R. Soc. Lond. B. Biol. Sci. *371*, 20150424.

Sanders-Bush, E., and Breeding, M. (1990). Serotonin1c receptor reserve in choroid plexus masks receptor subsensitivity. J Pharmacol Exp Ther *252*, 984–988.

1464 Sankaranarayanan, S., De Angelis, D., Rothman, J.E., and Ryan, T.A. (2000). The use of
1465 pHluorins for optical measurements of presynaptic activity. Biophys J *79*, 2199–2208.

1466 Saunders, N.R., Dziegielewska, K.M., Møllgård, K., and Habgood, M.D. (2018). Physiology and
1467 molecular biology of barrier mechanisms in the fetal and neonatal brain. J. Physiol. *596*, 5723–
1468 5756.

1469 Schwartz, M., and Baruch, K. (2014). The resolution of neuroinflammation in
1470 neurodegeneration: leukocyte recruitment via the choroid plexus. EMBO J. *33*, 7–22.

1471 Shechter, R., Miller, O., Yovel, G., Rosenzweig, N., London, A., Ruckh, J., Kim, K.-W., Klein,
1472 E., Kalchenko, V., Bendel, P., et al. (2013). Recruitment of Beneficial M2 Macrophages to
1473 Injured Spinal Cord Is Orchestrated by Remote Brain Choroid Plexus. Cell *38*, 555–569.

1474 Silva-Vargas, V., Maldonado-Soto, A.R., Mizrak, D., Codega, P., and Doetsch, F. (2016). Age-
1475 Dependent Niche Signals from the Choroid Plexus Regulate Adult Neural Stem Cells. Cell Stem
1476 Cell *19*, 643–652.

1477 Stasi, C., Sadalla, S., and Milani, S. (2019). The Relationship Between the Serotonin
1478 Metabolism, Gut-Microbiota and the Gut-Brain Axis. Curr. Drug Metab. *20*, 646–655.

1479 Strazielle, N., and Ghersi-Egea, J.F. (1999). Demonstration of a coupled metabolism-efflux
1480 process at the choroid plexus as a mechanism of brain protection toward xenobiotics. J Neurosci
1481 *19*, 6275–6289.

1482 Toda, T., Homma, D., Tokuoka, H., Hayakawa, I., Sugimoto, Y., Ichinose, H., and Kawasaki, H.
1483 (2013). Birth regulates the initiation of sensory map formation through serotonin signaling. Dev
1484 Cell *27*, 32–46.

1485 Tong, C.K., Chen, J., Cebrián-Silla, A., Mirzadeh, Z., Obernier, K., Guinto, C.D., Tecott, L.H.,
1486 García-Verdugo, J.M., Kriegstein, A., and Alvarez-Buylla, A. (2014). Axonal control of the adult
1487 neural stem cell niche. Cell Stem Cell *14*, 500–511.

1488 Urbina, F.L., Gomez, S.M., and Gupton, S.L. (2018). Spatiotemporal organization of exocytosis
1489 emerges during neuronal shape change. J Cell Biol *217*, 1113–1128.

1490 Wang, T., Ouzounov, D.G., Wu, C., Horton, N.G., Zhang, B., Wu, C.H., Zhang, Y., Schnitzer,
1491 M.J., and Xu, C. (2018). Three-photon imaging of mouse brain structure and function through
1492 the intact skull. Nat. Methods *15*, 789–792.

1493 Warf, B.C. (2005). Comparison of endoscopic third ventriculostomy alone and combined with
1494 choroid plexus cauterization in infants younger than 1 year of age: a prospective study in 550
1495 African children. J. Neurosurg. *103*, 475–481.

1496 Watanabe, M., Kang, Y.J., Davies, L.M., Meghpara, S., Lau, K., Chung, C.Y., Kathiriya, J.,
1497 Hadjantonakis, A.K., and Monuki, E.S. (2012). BMP4 sufficiency to induce choroid plexus
1498 epithelial fate from embryonic stem cell-derived neuroepithelial progenitors. J. Neurosci. *32*,
1499 15934–15945.

1500 Watson, J.A., Elliott, A.C., and Brown, P.D. (1995). Serotonin elevates intracellular Ca2+ in rat
1501 choroid plexus epithelial cells by acting on 5-HT2C receptors. Cell Calcium *17*, 120–128.

1502 Weisenburger, S., Tejera, F., Demas, J., Chen, B., Manley, J., Sparks, F.T., Martinez Traub, F.,
1503 Daigle, T., Zeng, H., Losonczy, A., et al. (2019). Volumetric Ca(2+) Imaging in the Mouse Brain
1504 Using Hybrid Multiplexed Sculpted Light Microscopy. Cell *177*, 1050-1066 e14.

Zhang, Y., Huang, G., Shornick, L.P., Roswit, W.T., Shipley, J.M., Brody, S.L., and Holtzman, M.J. (2007). A transgenic FOXJ1-Cre system for gene inactivation in ciliated epithelial cells. Am J Respir Cell Mol Biol *36*, 515–519.

Zheng, W., and Zhao, Q. (2002). Establishment and characterization of an immortalized Z310 choroidal epithelial cell line from murine choroid plexus. Brain Res *958*, 371–380.

Zheng, W., Zhao, Q., and Graziano, J.H. (1998). Primary culture of choroidal epithelial cells: Characterization of an in vitro model of blood-CSF barrier. Vitr. Cell. Dev. Biol. - Anim. *34*, 40–45.

Figure 1

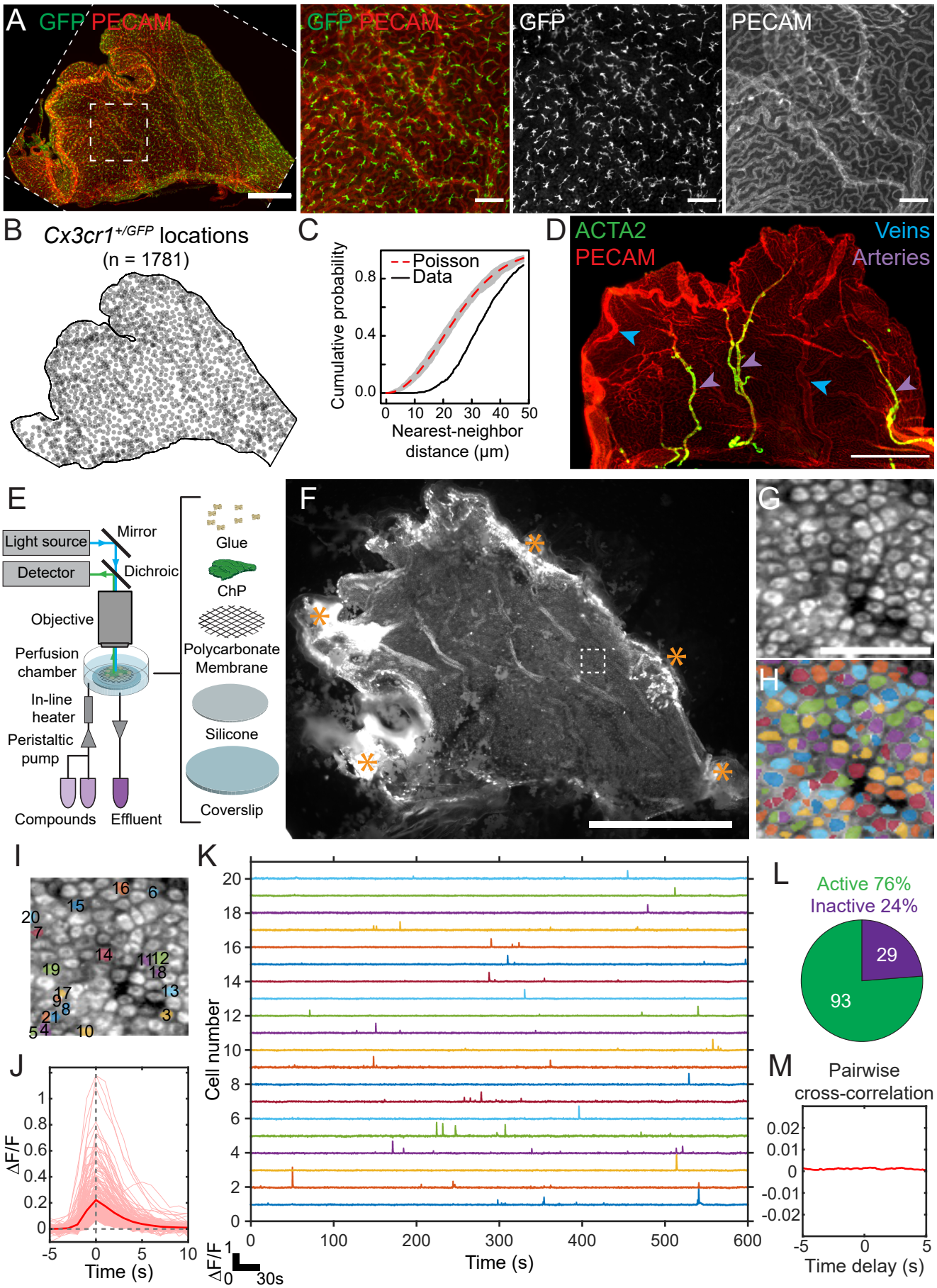
A
GFP PECAM
GFP PECAM
GFP
PECAM
B
Cx3cr1+/GFP locations
(n = 1781)
C
Poisson
Data
Cumulative probability
0.0
0.4
0.8
0 10 20 30 40 50
Nearest-neighbor distance (μm)
D
ACTA2
PECAM
Veins
Arteries
E
Light source
Mirror
Detector
Dichroic
Objective
Perfusion chamber
In-line heater
Peristaltic pump
Compounds
Effluent
Glue
ChP
Polycarbonate Membrane
Silicone
Coverslip
F
G
H
I
16 6 15 20 7 14 11 12 19 18 17 13 9 8 21 3 5 4 10
J
ΔF/F
Time (s)
K
Cell number
Time (s)
ΔF/F
30s
L
Active 76%
Inactive 24%
29
93
M
Pairwise cross-correlation
Time delay (s)

Figure 2

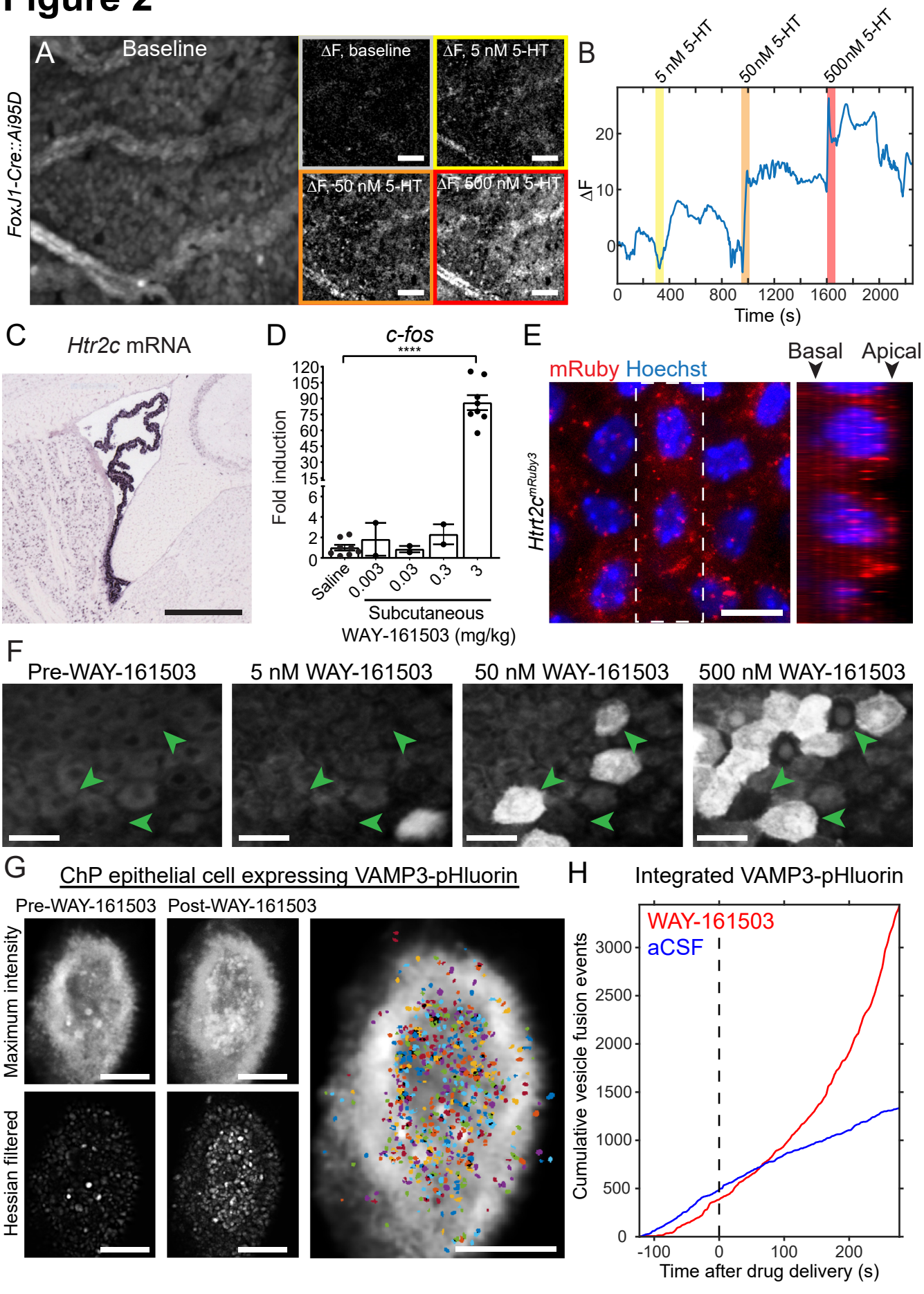
A
Baseline
FoxJ1-Cre::Ai95D
ΔF, baseline
ΔF, 5 nM 5-HT
ΔF, 50 nM 5-HT
ΔF, 500 nM 5-HT
B
5 nM 5-HT
50nM 5-HT
500nM 5-HT
ΔF
Time (s)
C
Htr2c mRNA
D
c-fos
****
Fold induction
Saline
0.003
0.03
0.3
3
Subcutaneous
WAY-161503 (mg/kg)
E
mRuby Hoechst
Basal
Apical
Htrt2c^mRuby3
F
Pre-WAY-161503
5 nM WAY-161503
50 nM WAY-161503
500 nM WAY-161503
G
ChP epithelial cell expressing VAMP3-pHluorin
Pre-WAY-161503
Post-WAY-161503
Maximum intensity
Hessian filtered
H
Integrated VAMP3-pHluorin
WAY-161503
aCSF
Cumulative vesicle fusion events
Time after drug delivery (s)

Figure 3

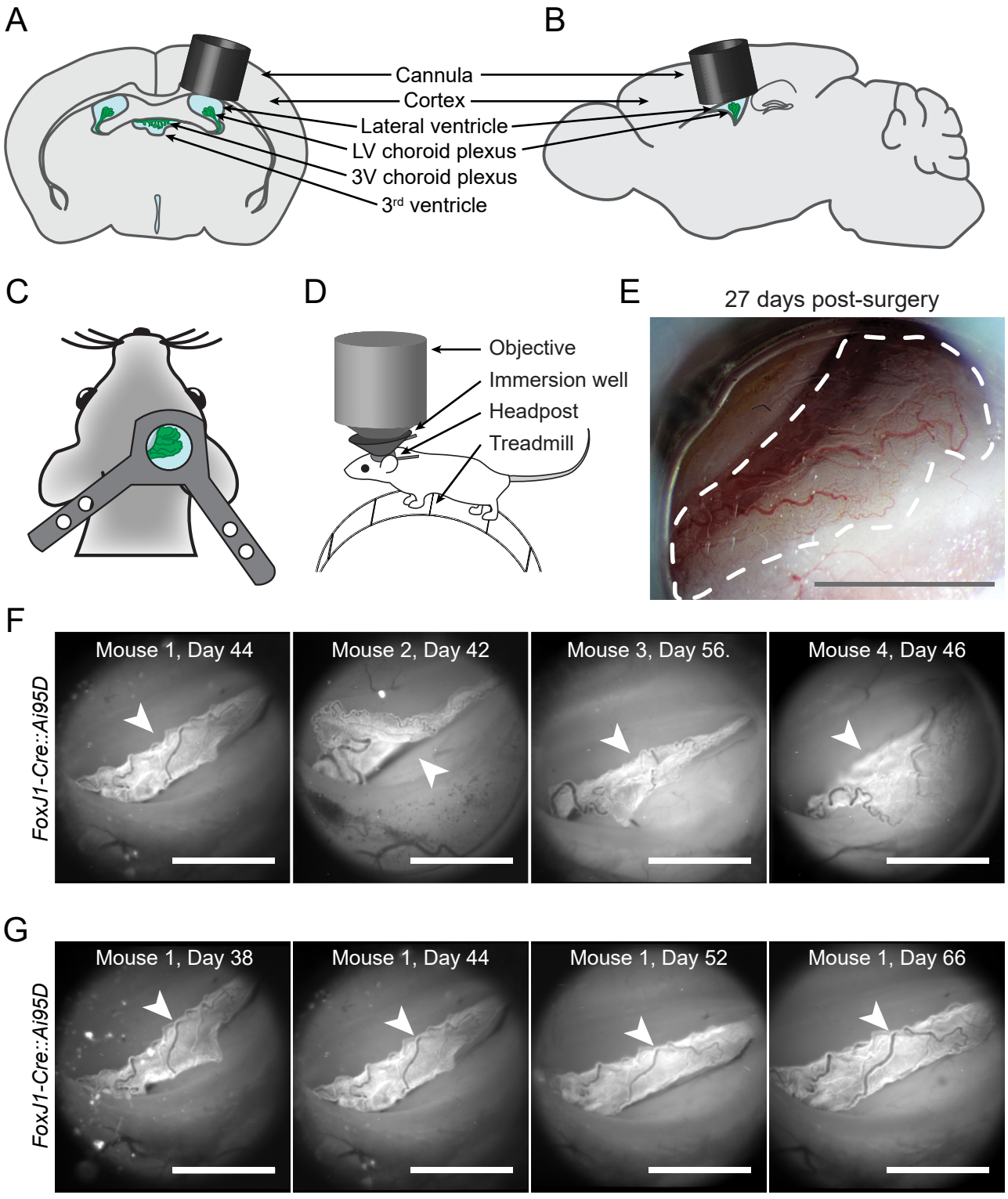
A
B
Cannula
Cortex
Lateral ventricle
LV choroid plexus
3V choroid plexus
3rd ventricle
C
D
Objective
Immersion well
Headpost
Treadmill
E
27 days post-surgery
F
FoxJ1-Cre::Ai95D
Mouse 1, Day 44
Mouse 2, Day 42
Mouse 3, Day 56.
Mouse 4, Day 46
G
FoxJ1-Cre::Ai95D
Mouse 1, Day 38
Mouse 1, Day 44
Mouse 1, Day 52
Mouse 1, Day 66

Figure 4

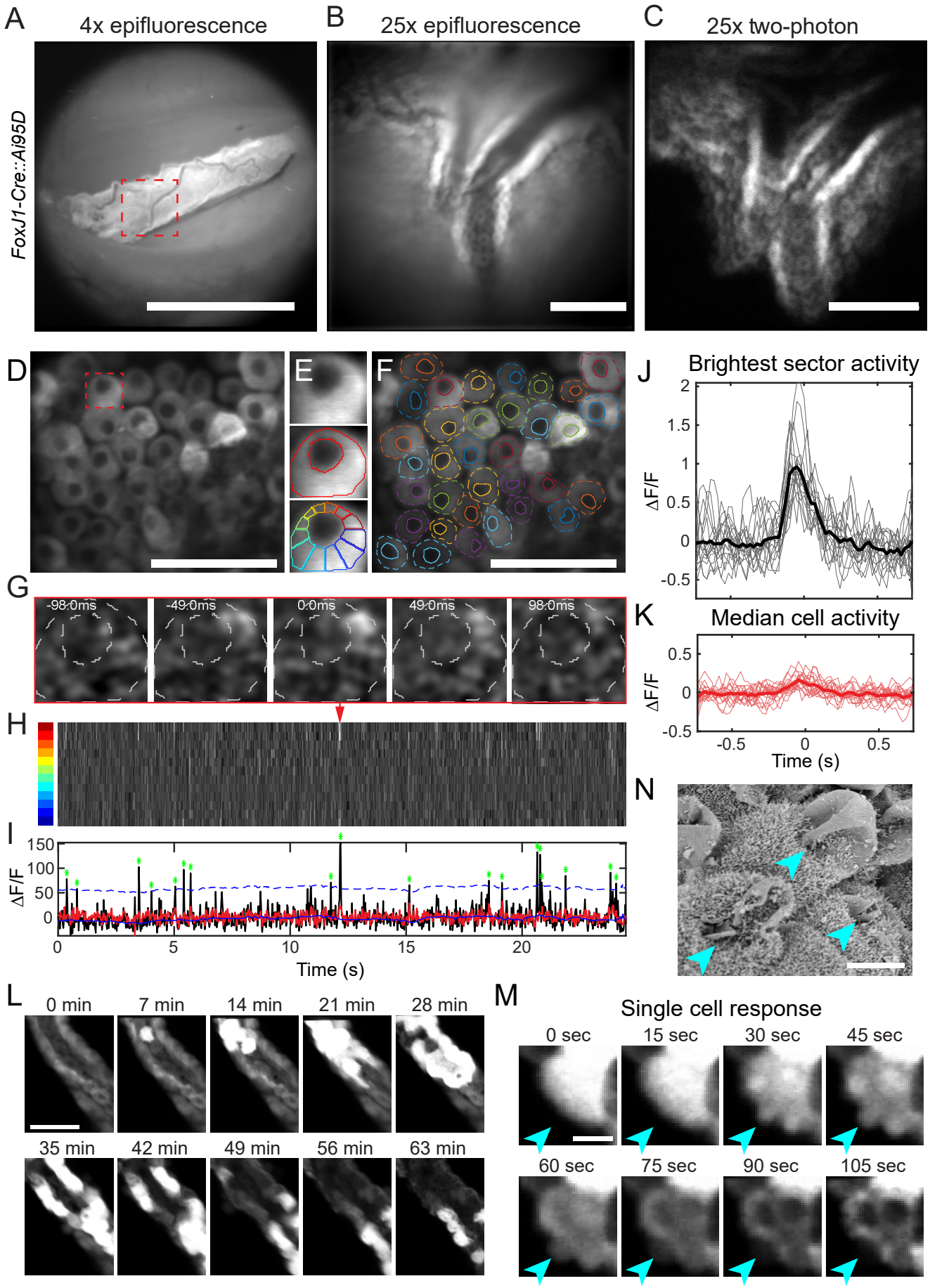
A
4x epifluorescence
B
25x epifluorescence
C
25x two-photon
FoxJ1-Cre::Ai95D
D
E
F
J
Brightest sector activity
ΔF/F
2
1.5
1
0.5
0
-0.5
G
-98.0ms
-49.0ms
0.0ms
49.0ms
98.0ms
K
Median cell activity
ΔF/F
0.5
0
-0.5
-0.5
0
0.5
Time (s)
H
I
ΔF/F
150
100
50
0
0
5
10
15
20
Time (s)
N
L
0 min
7 min
14 min
21 min
28 min
35 min
42 min
49 min
56 min
63 min
M
Single cell response
0 sec
15 sec
30 sec
45 sec
60 sec
75 sec
90 sec
105 sec

Figure 5

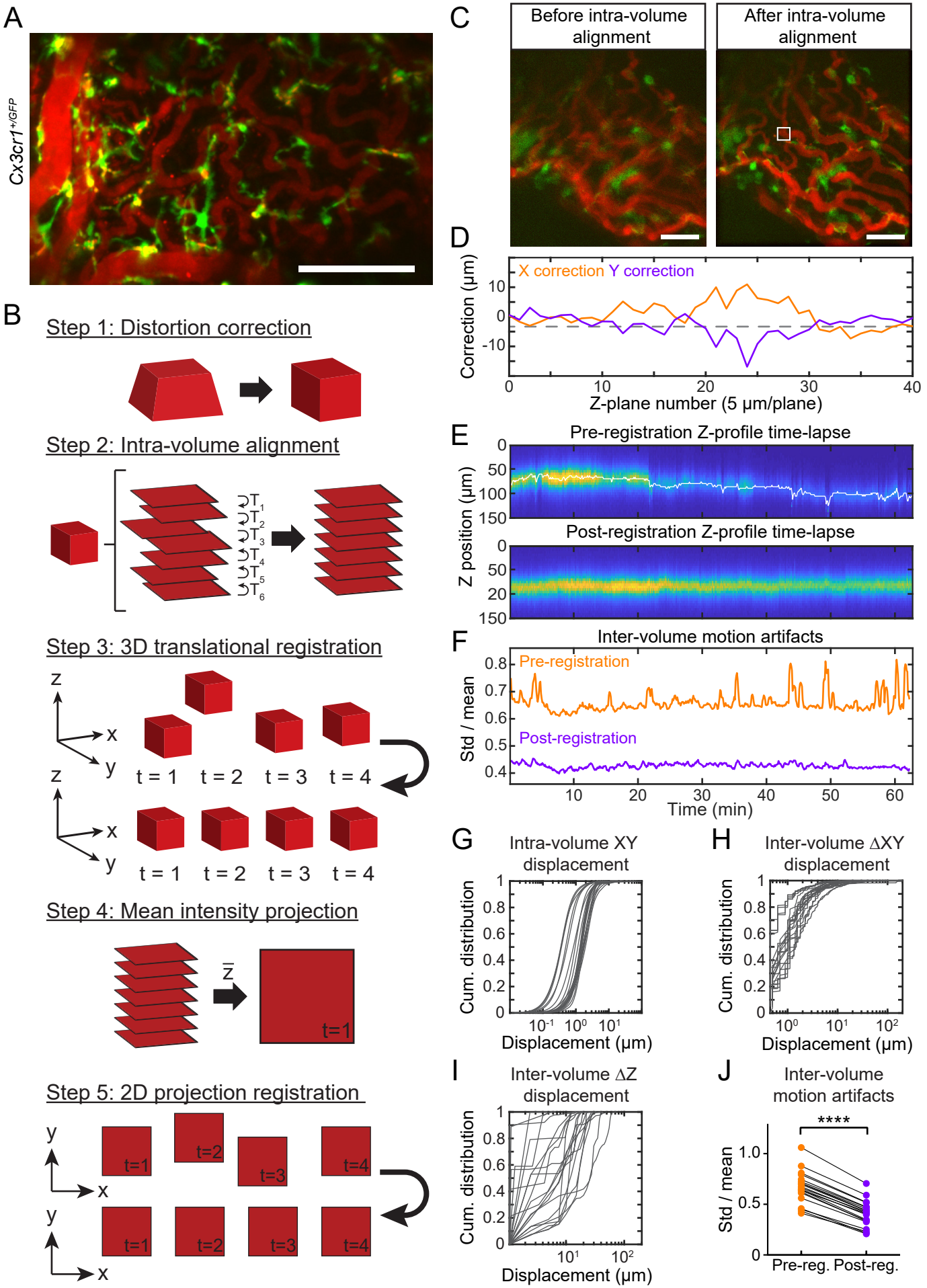
A
Cx3cr1+/GFP
B
Step 1: Distortion correction
Step 2: Intra-volume alignment
Step 3: 3D translational registration
t = 1
t = 2
t = 3
t = 4
Step 4: Mean intensity projection
Step 5: 2D projection registration
C
Before intra-volume alignment
After intra-volume alignment
D
X correction Y correction
Correction (μm)
Z-plane number (5 μm/plane)
E
Pre-registration Z-profile time-lapse
Post-registration Z-profile time-lapse
Z position (μm)
F
Inter-volume motion artifacts
Pre-registration
Post-registration
Std / mean
Time (min)
G
Intra-volume XY displacement
Cum. distribution
Displacement (μm)
H
Inter-volume ΔXY displacement
I
Inter-volume ΔZ displacement
J
Inter-volume motion artifacts
****
Pre-reg.
Post-reg.

Figure 6

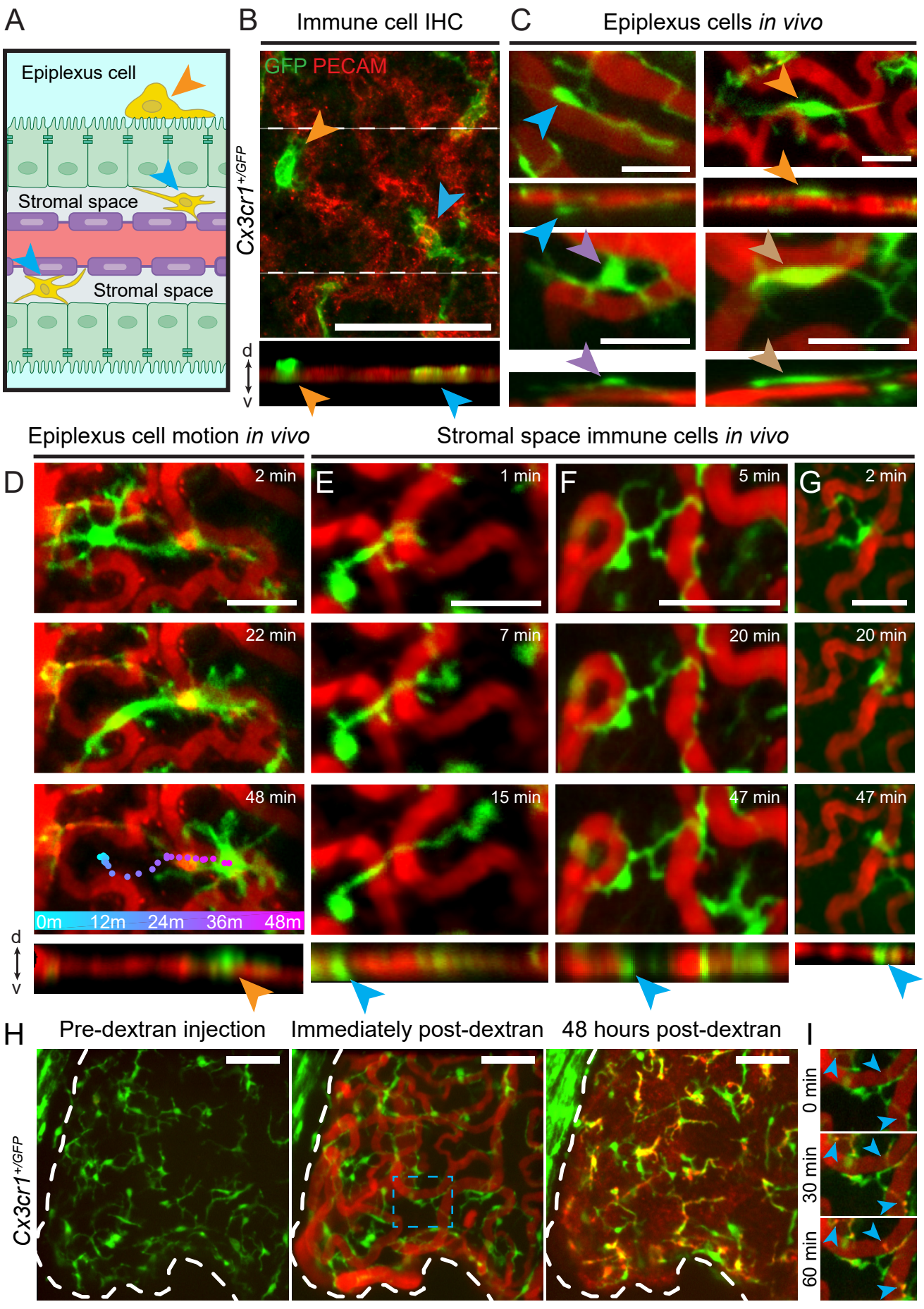
A
Epiplexus cell
Stromal space
Stromal space
B
Immune cell IHC
GFP PECAM
Cx3cr1+/GFP
d
v
C
Epiplexus cells in vivo
Epiplexus cell motion in vivo
Stromal space immune cells in vivo
D
2 min
22 min
48 min
0m 12m 24m 36m 48m
E
1 min
7 min
15 min
F
5 min
20 min
47 min
G
2 min
20 min
47 min
d
v
H
Pre-dextran injection
Immediately post-dextran
48 hours post-dextran
Cx3cr1+/GFP
I
0 min
30 min
60 min

Figure 7

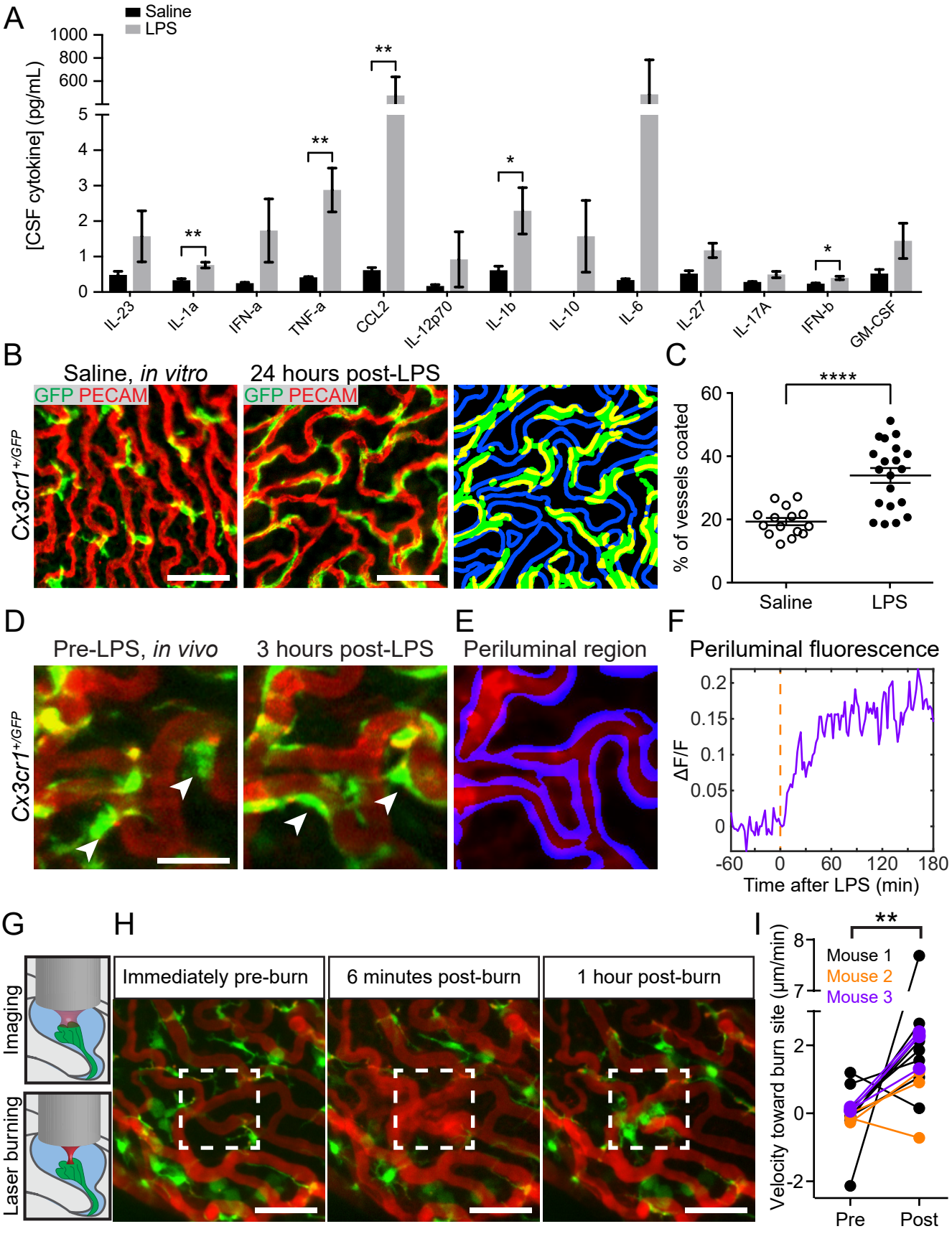
A
Saline
LPS
[CSF cytokine] (pg/mL)
1000
800
600
5
4
3
2
1
0
**
**
*
*
IL-23
IL-1a
IFN-a
TNF-a
CCL2
IL-12p70
IL-1b
IL-10
IL-6
IL-27
IL-17A
IFN-b
GM-CSF
B
Saline, in vitro
24 hours post-LPS
GFP PECAM
GFP PECAM
Cx3cr1+/GFP
C
****
% of vessels coated
60
40
20
0
Saline
LPS
D
Pre-LPS, in vivo
3 hours post-LPS
Cx3cr1+/GFP
E
Periluminal region
F
Periluminal fluorescence
ΔF/F
0.2
0.15
0.1
0.05
0
-60
0
60
120
180
Time after LPS (min)
G
Imaging
Laser burning
H
Immediately pre-burn
6 minutes post-burn
1 hour post-burn
I
**
Velocity toward burn site (μm/min)
8
7
2
0
-2
Mouse 1
Mouse 2
Mouse 3
Pre
Post